UNIVERSITAT POLITÈCNICA DE CATALUNYA
BARCELONATECH
Escola d'Enginyeria de Barcelona Est

MASTER'S THESIS

Master's degree in Materials science and engineering

MECHANICAL AND MICROSTRUCTURAL CHARACTERIZATION OF 3D PRINTED CERAMIC FUEL CELLS ELECTROLYTES

Report and Annexes

Author: Albert Folch Alcaraz
Director: Joan Josep Roa Rovira

Call for proposal: January 2020

Abstract

Nowadays, 3D printing (3DP) is leading a revolution of the processing technique, thanks to its versatility in the manufacture of complex geometries and having the ability to manufacture complex parts in one step, reducing both the manufacturing time and costs. With this technology, the aim is to bring science and society closer together, with the ultimate goal of developing new devices that are more efficient than the current ones in order to produce clean energy, since the fuel used is derived from hydrogen in contact with air to produce energy and water vapour. Specifically, in the field of energy and in particular by using this advanced methodology to 3DP solid oxide fuel cells is growing during the last decade. Therefore, in this sense, the solid oxide fuel cells (SOFCs) avoids the generation of greenhouse gases, such as CO_2, which is the ultimate global purpose to face the present worldwide climate crisis.

The purpose of this Master's thesis is the combination of these two fields, focusing on the electrolyte 3DP of SOFC, with the main objective to obtain the final material with microstructural and mechanical properties similar to those obtained by traditional techniques.

To carry out this study, two different geometries have been chosen, tubular and cylindrical, where the proportions of the printing material, processing conditions, etc. have been modified in order to achieve materials with a relative density higher than 96%, compared to traditional techniques, and mechanical properties similar to the materials produced by traditional routes, in this case, by using cold isostatic press (CIP). Within this context, the microstructural and mechanical properties have been determined by means of advanced characterization techniques, like: field emission scanning electron microscopy, nanoindentation, etc. Subsequently, the methodology of preliminary micro-compression of cylindrical and/or tubular fuel cells was determined.

To sum up, a density greater than 98% has been obtained with a hardness and elastic modulus of the 3DP electrolytes similar than those processed by using the conventional manufacturing techniques.

Resumen

Hoy en día, la impresión en 3D (3DP) está liderando una revolución en la técnica de procesamiento, gracias a su versatilidad en la fabricación de geometrías complejas y a la posibilidad de fabricar piezas complejas en un solo paso, reduciendo tanto el tiempo como los costes de fabricación. Con esta tecnología se pretende acercar la ciencia a la sociedad, con el objetivo final de desarrollar nuevos dispositivos más eficientes que los actuales para producir energía limpia, ya que el combustible utilizado se deriva del hidrógeno en contacto con el aire para producir energía y vapor de agua. Concretamente, en el campo de la energía y en particular mediante el uso de esta avanzada metodología para imprimir pilas de combustible de óxido sólido, ha crecido mucho durante esta última década. Por lo tanto, en este sentido, las pilas de combustible de óxido sólido (SOFC) evitan la generación de gases de efecto invernadero, como el CO_2, contra el cuál se está luchando a nivel mundial para hacer frente a la actual crisis climática.

El propósito de esta tesis de máster es la combinación de estos dos campos, centrándose en la impresión 3D del electrolito de las pilas de combustible, con el objetivo principal de obtener el material final con propiedades microestructurales y mecánicas similares a las obtenidas por las técnicas de fabricación tradicionales.

Para llevar a cabo este estudio se han elegido dos geometrías diferentes, tubular y cilíndrica, donde se han modificado las proporciones del material de impresión, las condiciones de procesamiento, etc., para conseguir materiales con una densidad relativa superior al 98%, en comparación con las técnicas tradicionales, y unas propiedades mecánicas similares a las de los materiales producidos por las vías tradicionales, en este caso, mediante el uso de prensa isostática en frío (CIP). En este contexto, las propiedades microestructurales y mecánicas se han determinado mediante técnicas avanzadas de caracterización, como: microscopía electrónica de barrido, nanoindentación, etc. Posteriormente, se ha determinado la metodología para ensayos de microcompresión de pilas de combustible cilíndricas y/o tubulares.

En resumen, se ha obtenido una densidad superior al 98% con una dureza y un módulo elástico de los electrolitos 3DP similares a los procesados mediante las técnicas de fabricación convencionales.

Acknowledgements

First of all, I would like to say that this Master's project has been the best way to close my academic stage in the Universitat Politècnica de Catalunya – BarcelonaTech (UPC) and the École Européenne d'Ingénieurs en Génie des Matériaux (EEIGM). It has been a long run, with ups and downs, but I have enjoyed it.

Secondly, I would like to express generous gratitude to my supervisor Joan Josep Roa for his guidance and help during the entire project and for having full confidence on my work. I would like to acknowledge to the PhD Student Joaquim Minguela, for helping me with the preparation of the cold isostatic press samples.

I would also like to mention and express gratitude to Laura Cabezas, who has given her disinterested assistance all along this project and has helped me with the 3D printer, and countless difficulties that we have faced together during this project.

In the same way, I would like to thank my colleagues Marc Serra and Oliver Giménez, and all my classmates for giving me moral support and accompanying me on this journey.

To finish, I am very thankful to my parents, my brother and especially Marta, for their constant support and for believing in me, not only during this four last months, but during all my academic journey.

Glossary of terms

AM: Additive manufacturing

CIP: Cold isostatic pressing

SOFC: Solid oxide fuel cell

YSZ: Yttria-stabilised zirconia

xY-TZP: Tetragonal zirconia partial stabilized with *x* molar percentage of yttria

AFC: Alkaline Fuel Cell

PEMFC: Proton Exchange Membrane Fuel Cell

PAFC: Phosphoric Acid Fuel Cell

MCFC: Molten Carbonate Fuel Cell

TT: Thermal treatment

OM: Optic microscope

SEM: Scanning electron microscopy

XRD: X-ray diffraction

H: Hardness

E: Elastic modulus

h: Displacement into surface

P: Applied load

Table of contents

1. Introduction

1.1. Fuel cells

Fuel cells are electrochemical devices that convert chemical energy (mainly fuels) into electrical energy directly, promising power generation with high efficiency and low environmental impact [1]. They are usually classified by the electrolyte employed in the cell. A second grouping is by the operating temperature for each of the fuel cells. Thus, there are low and high temperature fuel cells. Low temperature fuel cells are the Alkaline Fuel Cell (AFC), the Proton Exchange Membrane Fuel Cell (PEMFC, also called the Polymer Electrolyte Fuel Cell) and the Phosphoric Acid Fuel Cell (PAFC). The high temperature fuel cells operate at 500 - 1000 ^{o}C and are classed into two different types, the Molten Carbonate Fuel Cell (MCFC) and the Solid Oxide Fuel Cell (SOFC) [2]. All different types are presented below.

1.1.1. Low temperature fuel cells

- *Alkaline fuel cell (AFC):* The AFC works by the electrochemical combination of hydrogen and oxygen producing potable water, heat and electricity (see ***Figure 1.1***). The electrodes are separated by a porous matrix saturated with an aqueous solution, such as potassium hydroxide (KOH). They are among the most efficient fuel cells (70 %) but they only work with very pure gases, which is a major drawback in most applications. Another drawback is the poisoning of the fuel cell due to the not rejection of carbon dioxide (CO_2) that affects the KOH of the electrolyte [2].

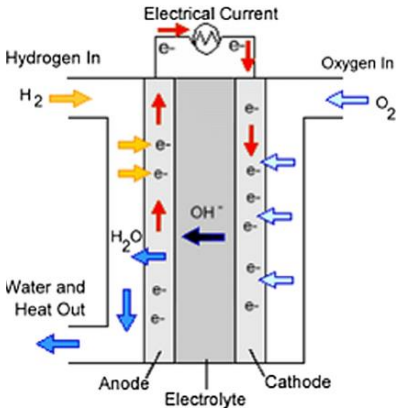

Figure 1.1. *Working schematisation of an AFC* [3].

- *Polymer electrolyte fuel cell (PEFC):* The PEFC use a proton-conducting polymer membrane as an electrolyte (see ***Figure 1.2***). They are low temperature fuel cells, operating at 85 – 105 ^{o}C and were the first to be used in space. A breakthrough in the field of PEFC came with the use of *Nafion* membranes (*DuPont*). These membranes possess a higher acidity, and consequently, higher conductivity than polystyrene sulfonate membranes used before. Their main application focuses on transportation due to their high power density [2].

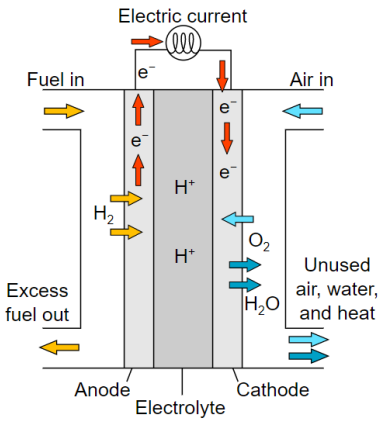

Figure 1.2. *Working schematisation of a PEFC* [3].

- *Phosporic acid fuel cells (PAFC):* The PAFC (see ***Figure 1.3***) is one of the most advanced system when it comes to commercial development. It is mainly used in stationary power plants to supply shopping malls and hospitals, for instance. The advantages of PAFC are its simple construction, its thermal, chemical, and electrochemical stability, and the low electrolyte volatility at operating temperatures (150 – 200 ^{o}C). The electrolyte is highly concentrated or pure liquid phosphoric acid (H_3PO_4) saturated in a silicon carbide (SiC) matrix [2].

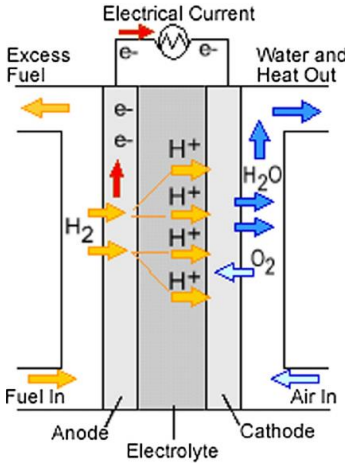

Figure 1.3. *Working schematisation of a PAFC* [3].

1.1.2. High temperature fuel cells

- *Molten carbonate fuel cells (MCFC):* This fuel cell uses a molten carbonate (usually a LiK or LiNa carbonate) electrolyte stabilised in a matrix ($LiAlO_2$), which can be supported with alumina (Al_2O_3) fibres for mechanical strength (see ***Figure 1.4***). MCFC systems can attain efficiencies of up to 50 % or up to 70 % when combining the fuel cell with other power generators. MCFCs can operate on a wide range of different fuels and are not prone to CO or CO_2 contamination, as is the case for low temperature cells [2].

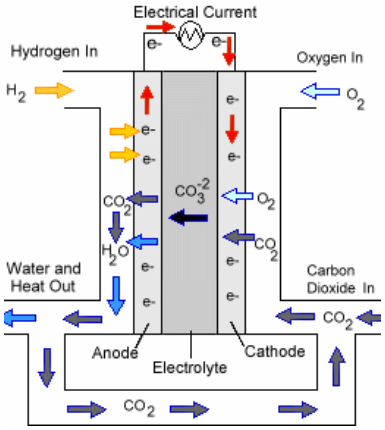

Figure 1.4. *Working schemematisation of a MCFC* [3].

- *Solid oxide fuel cells (SOFC):* SOFCs (see ***Figure 1.5***) employ a solid oxide material as electrolyte and are, thus, more stable than MCFCs because no leakage problems, due to liquid electrolytes, can occur. SOFCS in combination with co-generation cycles, also provide a high efficiency (up to 70 %). It is difficult to find suitable materials which have the necessary thermal and chemical stability properties for operating at high temperatures [2]. More information about the materials used as electrolyte, cathode and anode is described in ***section 1.2***.

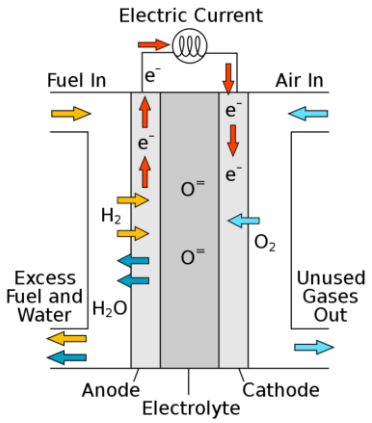

Figure 1.5. *Working schematisation of a SOFC* [3].

1.2. Solid Oxide Fuel Cells

A solid oxide fuel cell (SOFC) is a ceramic device that is used to convert chemical energy to electrical energy. In order to do so, SOFC use gases as reactants, usually hydrogen as a fuel and oxygen as oxidant. The main characteristic of SOFC is that the electrolyte is in a solid state, contrary to electrochemical cells which is in liquid state, for instance. The electrolyte is an oxide metal which needs to work between 600 to 1000ºC where ceramics become ionic conductors. Some of the advantages of using a solid-ceramic electrolyte are the elimination of corrosion and a better mechanical performance that enhanced lighter and more compact structures, unachievable in fuel cells systems having liquid electrolyte. However, there still some limitations linked to processing techniques and working temperatures. For this reason, researchers are trying to develop a suitable pair of materials (electrolyte/anode and electrolyte/cathode) with high adherence properties and similar thermal coefficient expansion, in order to reduce residual stresses at the interphase generated by thermal fatigue (cooling-heating cycles). Further information of each part of a SOFC and its characteristics is explained in ***section 1.2.1*** and found in [4].

1.2.1. Parts: Electrolyte, anode and cathode

A ceramic fuel cell is a device that consists of two electrodes separated by a solid electrolyte. Fuel is fed to the anode, where it oxidizes and releases electrons to the external circuit. Oxidant is fed to the cathode, accepts the electrons from the external circuit and undergoes a reduction reaction, see ***Eq.1.1*** and ***Eq.1.2*** to understand the chemical process. The electron flow from the anode to the cathode produces direct-current electricity.

$$H_2 \rightarrow 2H^+ + 2e^- \qquad \textbf{(Eq. 1.1)}$$

$$\frac{1}{2}O_2 + 2e^- \rightarrow O^{2-} \qquad \textbf{(Eq. 1.2)}$$

In theory, any gases capable of being electrochemically oxidized and reduced can be used as fuel and oxidant in a fuel cell, following the scheme of the process in ***Figure 1.6***.

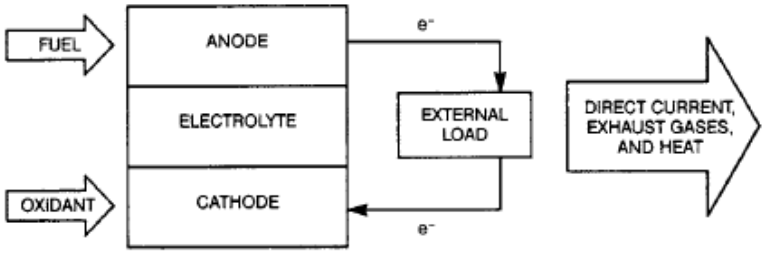

Figure 1.6. *Working scheme of a fuel cell [4].*

However, hydrogen is currently the most common fuel, since it has high electrochemical reactivity and can be derived from common fuels such as hydrocarbons, alcohols, or coals. Oxygen is the most common oxidant, since it is readily and economically available from air, as reported on [5].

Fuel cells have the characteristic of modularity which means that cells can be made in modular sizes. Thus, they can be easily increased or decreased. Since the efficiency of fuel cells is not dependant of size, they can be designed in different shapes and sizes to be suitable for the desirable application. Hence, practical SOFCs are not operated in single units, rather, they are connected using a component named interconnect, which connects the anode of one cell to the cathode of the next cell, forming what is referred to as a stack, which increases significantly the overall efficiency of the cell [5].

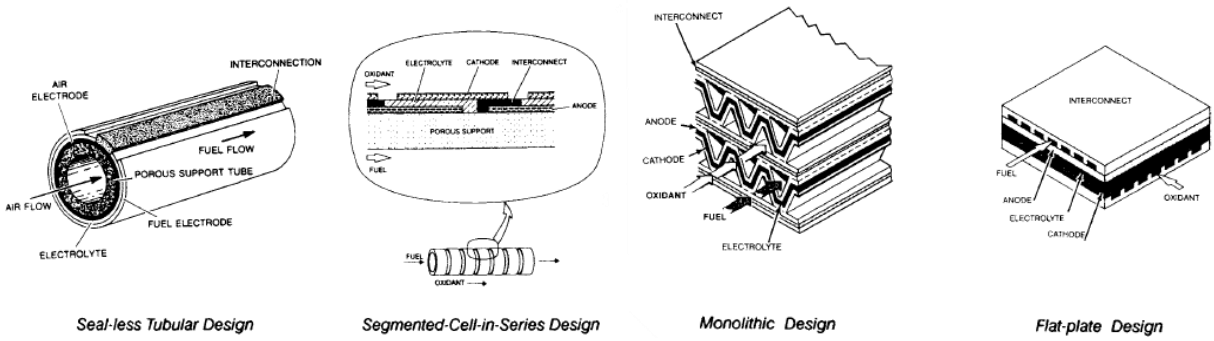

Figure 1.7. *Different possible form factors for fuel cells [5].*

Stacks can be configured in series, parallel or both combinations. There exist different form factors depending on the application, as depicted in ***Figure 1.7.***

The main physical and chemical characteristics such as; mechanical properties, conductivity and thermal properties of each part are summarized on ***Table 1.1.***

Table 1.1. *Physical and chemical characteristics of the four components of a SOFC [5].*

	Requirements				
	Conductivity	**Stability**	**Compatibility**	**Porosity**	**Thermal Expansion**
Electrolyte	High ionic conductivity Negligible electronic conductivity	Chemical, phase, morphological, and dimensional stability in fuel and oxidant environments	No damaging chemical interactions or interdiffusion with adjoining cell components	Fully dense	Thermal expansion match with adjoining components
Cathode	High electronic conductivity	Chemical, phase, morphological, and dimensional stability in oxidant environment	No damaging chemical interactions or interdiffusion with adjoining cell components	Porous	Thermal expansion match with adjoining components
Anode	High electronic conductivity	Chemical, phase, morphological, and dimensional stability in fuel environment	No damaging chemical interactions or interdiffusion with adjoining cell components	Porous	Thermal expansion match with adjoining components
Interconnect	High electronic conductivity Negligible ionic conductivity	Chemical, phase, morphological, and dimensional stability in fuel and oxidant environments	No damaging chemical interactions or interdiffusion with adjoining cell components	Fully dense	Thermal expansion match with adjoining components

1.2.2. Characteristics and requirements

All types of fuel cells must present the following characteristics in order to perform correctly [4]:

i. *High conversion efficiency*: The main feature of a fuel cell is its high conversion chemical to electrical efficiency (45-60%). A fuel cell converts the chemical energy of the fuel directly into electrical energy. Hence, losses involved in the conversion of fuel to heat, to mechanical energy, and then to electrical energy are avoided.

ii. *Environmental compatibility*: Emissions of pollutants from fuel cells are several orders of magnitude lower than those produced by conventional power generators. Emissions of NO_x, SO_x, and other high pollutants is negligible for fuel cell systems.

iii. *Modularity*: Fuel cells have the characteristic modularity, which means cells can be made in different sizes. Thus, fuel cell size can be easily increased or decreased. Since the efficiency of a fuel cell is relatively independent of size, fuel cells can be designed and tailored for different applications, as seen in ***Figure 1.8***.

iv. *Sitting flexibility*: Due to its modularity, fuel cells can be placed at different locations with minimum siting restrictions. Fuel cells operation is quiet because they have no moving parts; the only noises are those from auxiliary equipment. Thus, fuel cells can be easily placed near urban residential areas.

v. *Multifuel capability*: Certain types of fuel cells have multifuel capability. High-temperature fuel cells can process hydrocarbon fuels internally with no need of subsystems to process conventional fuels into simple forms.

Figure 1.8. *Different applications of fuel cells; a) Fuel cell in the Toyota Mirai model [6] and, b) a fuel cell for ships as part of a maritime project for the U.S. Department of Energy [7].*

1.3. SOFCs materials

1.3.1. Electrolyte materials

In this Master's thesis will only be studied the materials concerning the electrolyte. For further information about which materials are used for the anode and the cathode, see Refs.[5, 6].

In SOFCs, stabilized Zirconia based ceramic materials has been the most as electrolyte because of its oxygen-ion conductivity and stability in both oxidizing and reducing atmospheres. The Y_2O_3-stabilized material (YSZ) is the most common. However, other oxides as: doped ceria, stabilized bismuthsesquioxide and protonic conductors can be considered depending on the working conditions [10].

1.3.1.1. Zirconium oxide

Zirconia (ZrO_2) is characterized by distinct crystallographic structures, characterizing a property known as polymorphism. It presents three different crystal structures: monoclinic (*m*), tetragonal (*t*) and cubic (*c*), (see ***Figure 1.9***). Pure zirconia has a monoclinic structure at room temperature, which is stable up to 1170 °C. Then, the monoclinic structure changes to tetragonal and to cubic fluorite structure above 2370 °C. This last one exists up to the melting point of 2680 °C [11].

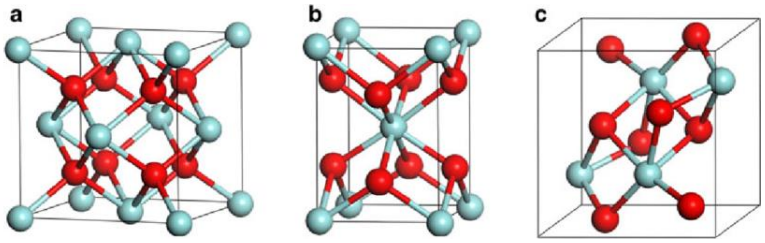

Figure 1.9. *Crystal structures of ZrO2: (a) Cubic, (b) tetragonal and (c) monoclinic. Red and blue spheres correspond to oxygen and zirconium atoms, respectively [12].*

The monoclinic/tetragonal (m→t) phase transformation is thermodynamically reversible, but it presents a volume change (3 to 5%): contraction on heating and expansion on cooling. Stresses generated by the expansion originate cracks in pure zirconia ceramics that, after sintering break into pieces. The addition of stabilizing oxides like CaO, MgO, CeO_2 or Y_2O_3, allows the generation of a multiphase material known as partially stabilized zirconia (PSZ), which presents a *c*-$Zr0_2$ microstructure at room temperature with *t*- and *m*- precipitates. These precipitates improve the mechanical properties of PSZ thanks to the phase transformation of (t→m), causing a volume expansion that stops crack propagation. This mechanism is called phase transformation toughening (see ***Figure 1.10***) and is responsible for the high toughness associated with PSZ.

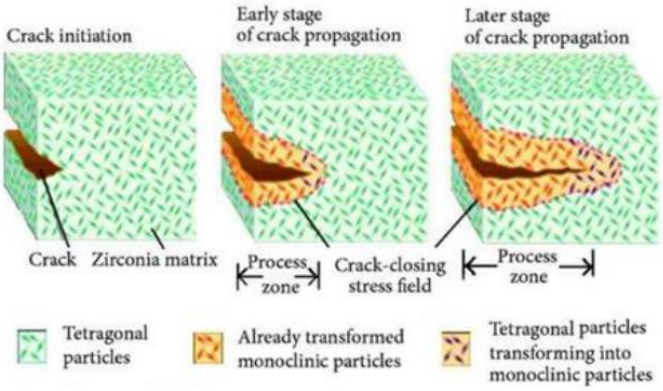

Figure 1.10. *Toughening mechanism induced during the t→m phase transformation [13].*

This property is characteristic of the Y_2O_3-stabilized material with 3% mol., also called yttria-tetragonal (3Y-ZrO_2) and it is used as a biomaterial for dental implants [14].

However, PSZ presents another phase transformation mechanism that has a negative impact on its mechanical properties. The so-called hydrothermal degradation is the mechanism responsible for most failures of PSZ components in service. This phenomenon occurs at low temperatures within a range of 65 to 500 ^{o}C and is caused by the humidity of the environment. Water molecules enhance the t→m phase transformation in the material's surface and further propagation inside of the material, leading to cracks formation [11].

Among the various stabilized zirconia, the Y_2O_3-stabilized material with 3 to 10% mol. are the most used compositions. The fraction of *t*-ZrO_2 phase at room temperature is dependent of the size of grains and on the yttria content. Hence, the t→m phase transformation of grains can be inhibited in a fine grained structure and above a certain yttria content [14]. Respecting these two conditions it can be possible to obtain **fully stabilized cubic zirconia**. In order to do so, the minimum yttria content is 8 to 10% mol. (see ***Figure 1.11***). Fully stabilized zirconia exhibits better ionic conductivity, and avoids problems associated with phase transformation achieving a higher mechanical stability. Thus, these properties become more interesting for SOFC applications.

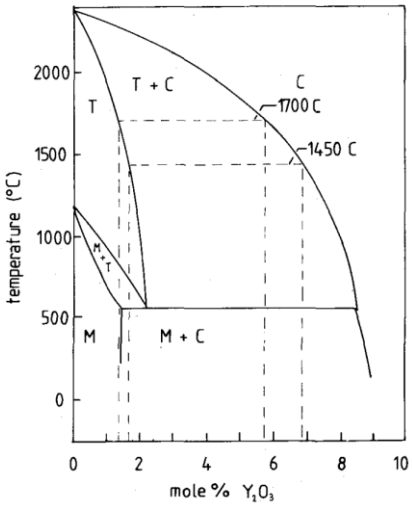

Figure 1.11. *Phase diagram of ZrO_2-Y_2O_3 [15].*

1.4. Manufacturing techniques

Ceramic materials have always had limitations because of manufacturing difficulties caused by their properties. Due to a high melting point, high Young's modulus and high hardness, melt-shaping processes and machining techniques are not suited for ceramic components. Hence, complex shape components are challenging and expensive to produce. However, the invention of additive manufacturing has opened a lot of possibilities in terms of forms and designs that engineers were not able to accomplish before. In this section and along ***section 1.4.2.*** a comparison between traditional manufacturing techniques and advanced techniques such as additive manufacturing technique will be discussed in detail [16][17].

1.4.1. Traditional techniques

i. ***Uniaxial and isostatic pressing***: these techniques consist on applying a constant pressure to the powder in order to compact it in the desired shape. Is applied for producing relatively simple-shaped parts in large series. Only a few organic additives are necessary for reducing the powder friction in the pressing die and for providing a certain green strength to the powder compact. Moreover, these processes are often combined with a subsequent green machining process such as milling for producing complex-shaped parts. However, a remarkable disadvantage of this shaping method can be seen in the waste of valuable material. Up to 90% of the material is removed in the milling process. An application of this technique are dental implants.

ii. ***Tape casting:*** Tape casting is based on an aqueous or nonaqueous slurry, which is cast to a moving tape by slot dies or curtain coating technologies. Ceramic limb green tapes can be

corrugated, coiled or wrinkled owing to a certain amount of organic binders and plasticizing agents. This technique is suitable for manufacturing wide, thin and even products or semi-products. It is established as a large-series production method for electronic wafers or microelectromechanical systems.

iii. ***Slip casting:*** This processing technology is a more classic shaping route known from traditional ceramics and porcelain products. This wet-shaping technology starts from aqueous slurries, which are poured into a plaster mould. Due to the porosity of the gypsum, capillary forces draw the suspension medium water into the mould. The powder particles, which cannot enter the pore channels, form a solid layer at the mould surface. After certain increase of the layer thickness, the residual slurry is removed from the mould. After a short drying time, the mould is opened, and the green part can be taken out of the mould for further drying and final sintering. The advantage of this wet-shaping technology is the ability to manufacture very complex-shaped parts. However, the plaster mould has a relatively short lifespan.

iv. ***Extrusion:*** This technology allows producing tubes, honeycomb structures or multichannel structures like filtration membranes. Together with injection moulding, it is one of the two main (thermo)plastic shaping methods for ceramics. For this process, the ceramic powder must be mixed with a thermoplastic organic binder. The powder mixture is called feedstock. Extrusion is carried out in piston extruders or vacuum screw extruders equipped with a die, providing the final shape of the product. The die is an expensive tool made of hard metal because of the very abrasive ceramic particles in the feedstocks. Despite all the products that can be made with this technology, the main disadvantage is given by the fact that the shape in *z*-direction is fixed.

v. ***Ceramic injection moulding:*** Ceramic injection moulding (CIM) is the shaping process for large-series production of components with high geometrical complexity. Holes and undercuts, microstructures, thin walls, and free-formed surfaces can be made without a further mechanical treatment. Some examples of ceramic components produced by CIM are ceramic turbo chargers, microturbines, watch housings, and thread guides for textile industry. This technology is adequate independently from the ceramic material. Moreover, it allows combining different materials with different properties via multicomponent injection moulding. The shaping method work almost as waste-free, because defect green parts can be recycled. The limited flexibility of tooling and the high costs of it are the main reasons why CIM only makes sense for medium or large productions, though.

1.4.2. Advanced techniques: Additive manufacturing

Along this section, a brief explanation of the main 3D printing routes will be explained:

i. ***Powder bed binder jet/inkjet 3D printing:*** this process is one of the most traditional three-dimensional (3D) additive manufacturing (AM) technologies that was invented in 1993 at Massachusetts Institute of Technology (*MIT*). Since then, the technology has been used for fabrication of plaster-based ceramic materials. In this process, the powder is spread in thin layers (usually 80 to 150 µm) on top of a solid platform and selectively bonded by the action of an inkjet print head, which contain a liquid binder or solvent. The unbound powder is removed by blowing or vacuuming. Depending on the type of ceramic powder used, the produced parts will undergo postprocessing such as sintering or infiltration to improve mechanical and physical properties. It must be mentioned that although printed material in plaster-based printers is a ceramic material, if impregnated with and adhesive, it will not be a pure ceramic but a polymer-ceramic composite. As no extreme heating is required during and after processing, colours can be added to the part (see ***Figure 1.12***).

Figure 1.12. *Examples of powder bed binder jet/inkjet 3D printed parts [16].*

One of the main *disadvantages* of this technique is that it is almost impossible to fabricate fully dense ceramic as no force is applied to pack the ceramic particles. This will make the sintering process almost ineffective for densification of the component. However, remaining porosity of the final part can be useful for biomedical applications such as 3D printed scaffolds made of tri-calcium phosphate and hydroxyapatite.

ii. ***Selective Laser Melting:*** This is a 3D process in which a powder is sintered or melds by the utilization of a CO_2 laser beam (see ***Figure 1.13***). The chamber is heated to nearly melting point of the material. The laser binds the powder layer by layer. The particles lie freely in a bed,

which is controlled by a piston that is lower down same amount of the layer thickness every time a layer is done. This process offers a great variety of materials that could be used: plastic, metals, combination of metals and combinations of metals and ceramics. No post-curing is required, and the unused powder can be recycled. The *disadvantages* are that the accuracy is limited be the size of particles of the material, oxidation needs to be avoided by executing the process in an inert gas atmosphere and temperature has to be near the melting point.

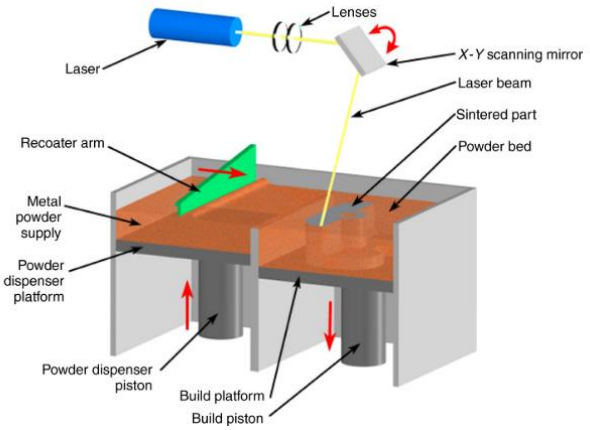

Figure 1.13. *Schematic representation of Selective Lase Melting process [16].*

iii. ***Stereolithography (SLA):*** This 3D printing methodology is the most widely used and the first rapid prototyping technology invented. The basic principle of the process is to solidify a photocurable resin using a UV laser source and build up the object using layer-by-layer deposition method. There exist two different types of SLA process: top-down system and bottom-up system.

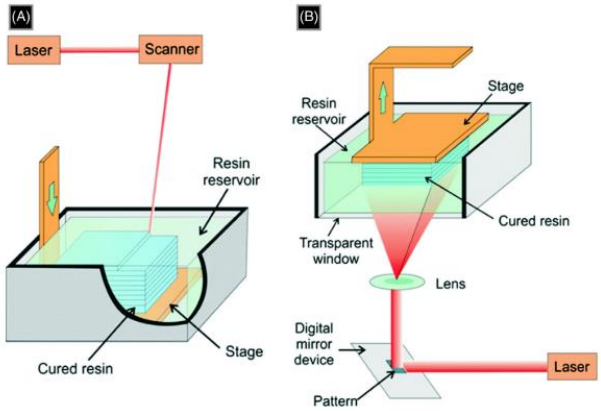

Figure 1.14. *Schematic representation of SLA process; (A) Top-down system, (B) Bottom-up system [16].*

a) *Top-down system*: Top-down SLA systems are using low-power, highly focused UV laser beam to scan successive cross-sections of the object in a tank of liquid photosensitive polymer, see ***Figure 1.14 (A)***. As the laser traces the layer, the

polymer solidifies, and the excess areas are left as liquid. After the platform sank down for the next layer, a blade is moved across the surface to smooth it. The platform is lowered by a distance equal to the layer thickness and the process start again.

b) *Bottom-up system*: Bottom-up systems use a LED lamp in conjunction with a liquid crystal display panel, which exposes an entire layer of photopolymer at one time. Cured layers are pulled out of the liquid and the process is ready for the next layer, see ***Figure 1.14 (B)***. In addition to avoiding the use of expensive lasers, this method has the advantage of not requiring a large quantity of photopolymer, reducing the cost of the process.

The manufacturing process requires the formulation of a photoreactive medium containing a photocurable resin and powders. The organic phase is removed by a thermal treatment and followed by a sintering stage to ensure the final properties of the ceramic piece. Its *advantages* are good surface finish and high accuracy, which can be seen in ***Figure 1.15***.

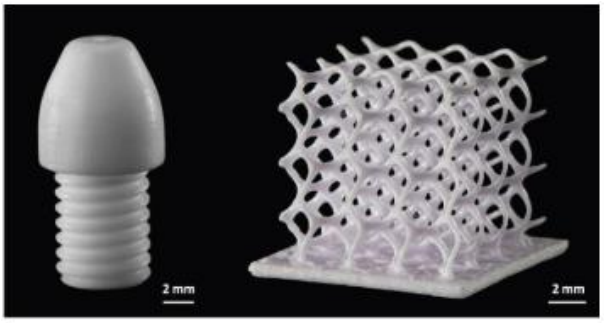

Figure 1.15. *Examples of ceramic parts manufactured by SLA [16].*

iv. ***Robocasting:*** This process consists on extruding through one or more heads a viscous ceramic paste comprised of ceramic powder charge and a suspension medium. Rheological properties of the filament are critical to minimize the deformation of the part and provide good interfilament bonding. In this technique, the ceramic paste undergoes a transformation from a pseudoplastic to a dilatant behaviour upon extrusion through the nozzle. This happens through partial drying of the paste.

Due to the high particle packing density achieved, the mechanical properties of the parts obtained are generally greater than those of similar geometries printed through other AM techniques. However, this process is limited by two key factors; the diameter size of the nozzle, which depends on the ceramic particle size of the paste, and the fact that this process consists in the extrusion of independent yarns that make the structure a discontinuous fabric. To fully

densify the material and eliminate the polymer matrix, a thermal treatment is needed. Its main *advantage* are the easiness of the process and the equipment.

1.4.3. Advantages and disadvantages

Compared to conventional manufacturing techniques, AM techniques have the following **advantages** [17]:

i. *Material efficiency:* Unlike conventional subtractive manufacturing where large amount of materials needs to be removed, AM uses raw materials efficiently by building parts layer by layer. Leftover materials can often be reused.
ii. *Resource efficiency:* Conventional processes require auxiliary resources such as jigs, cutting tools, and coolants in addition to the main machine tool. AM does not require these additional resources. As a result, parts can be made by small manufacturers that are close to customers.
iii. *Part flexibility:* Because there are no tooling constraints, parts with complex features can be made in a single piece. In addition, it is possible to build a single part with varying mechanical properties. This opens opportunities for design innovation.
iv. *Production flexibility:* AM machines do not require costly setups which means they are economical in small batch production. Production can be easily synchronized with customer demand. In addition, problems regarding production bottlenecks are eliminated because complex parts are produced in single pieces.

However, AM technology still cannot fully compete with conventional manufacturing, especially in the mass production field because of the following **drawbacks** [17].

i. *Size limitations:* AM processes often use liquid polymers, or a powder comprised of resin or plaster, to build object layers. This fact renders AM unable to produce large-sized objects due to lack of material strength. Large-sized objects also often are impractical due to the extended amount of time needed to complete the building process.
ii. *Imperfections:* Parts produced using AM often present a rough surface finish. This appearance is due to plastic beads or large-sized powder particles that are stacked on top of each other, giving the end product an unfinished look.
iii. *Cost:* AM equipment is considered an expensive investment. Entry level 3D printers average approximately 3.000 € and higher-end models up to 30.000 €.

1.5. State of the art

On this Master's thesis, two main fields may be covered: *The first one and more general is the generation of the SOFC's electrolytes by means of AM methodology and in particular using robocasting technique, and the second one is the characterisation of the material used for this component (8YZTP).*

Since the use of 8YZTP as SOFC's electrolytes and robocasting as AM technique are relatively new fields of investigation, only a few articles are available on the subject. However, investigations concerning the different aspects taken separately can be found more easily. In addition, some articles concerning the SOFCs functioning ways and requirements, and some concerning the different current AM techniques will be briefly presented.

Here, some examples of articles covering the different fields are briefly summarized. All these projects will lead to a better understanding of the main goal of this Master's thesis.

Ellen Ivers-Tiffée, André Weber, Dirk Herbstritt, *Materials and technologies for SOFC-components,* Journal of the European Ceramic Society 21 (2001) 1805-1811.

On this article are detailed the different areas of SOFCs applications, which materials are used for each part of the fuel cell and the material requirements. It also presents the different types of SOFCs depending on the operating temperatures. The YSZ and TZP are cited as possible candidates to be used as electrolytes since they present many advantages compared to the other possible materials, such as an excellent mechanical stability (3YSZ), excellent stability in oxidizing and reducing environment and good ion conductivity (8YTZP).

Zhangwei Chen, Ziyong Li, Junjie Li, Chengbo Liu, Changshi Lao, Yuelong Fu, Changyong Liu, Yang Li, Pei Wang, Yi He, *3D printing ceramics: A review,* Journal of the European Ceramic Society 39 (2019) 661-687.

This article is a review of the different AM techniques used to manufacture ceramic parts. It helps to understand the advantages and disadvantages of every technique and the materials that are better for each one. Robocasting technique is also explained.

J. C. Ruiz-Morales, A. Tarancón, J. Canales-Vázquez, J. Méndez-Ramos, L. Hernández-Afonso, P. Acosta-Mora, J. R. Marín Rueda and R. Fernández-González, Three dimensional printing of components and functional devices for energy and environmental applications, Energy Environ. Sci. (2017), 10, 846.

This article is a review of different 3D printing technologies for the fabrication of functional components and devices for energy and environmental applications. More specific, it explains the

different additive techniques developed for SOFCs and which printing technology is more accurate for each part of SOFCs (anode, cathode and electrolyte).

Cesarano, J. *A Review of Robocasting Technology*, MRS Proceedings (1998) 542, 133. doi:10.1557/PROC-542-133

This is a review of the robocasting AM technology. It presents the main characteristics that a ceramic slurry must meet in order to fit robocasting technique. It also explains the rheology requirement of the paste to achieve the best result, which is important to a good understanding of how this technique works.

E.Feilden, E.García-tuñón Blanca, F.Giuliani, E.Saiz, L. Vandeperre, *Robocasting of structural ceramic parts with hydrogel inks,* Journal of the European Ceramic Society 36 (2016) 2525-2533.

On this article, an extensive explanation of the robocasting technique is done. However, the real interest of it is that it explains the formulation of hydrogels inks, which is an important part of this Master's thesis.

It stablishes that the real advantage of robocasting lies in the mechanical quality of the material produced and the flexibility of the technique to print different materials. Full densification of robocasted parts has been readily demonstrated with conventional processing of the green parts. Nevertheless, reports of their mechanical properties are quite scarce in the literature, and no analysis of the reliability of the parts seems to have been completed. This article reports the mechanical properties of printed parts for both oxide (Al_2O_3) and non-oxide ceramics (SiC). Almost fully dense printed parts were reported and good mechanical properties of both materials, it also reports the morphology of defects that limited the mechanical properties. In addition, a rheological study of the Al_2O_3 ink is made and it is proved to be optimum for robocasting.

Although these are not the materials used in the project, it is important to take into account as a better understanding for the interpretation of the results.

Erwin Peng, Xiangxia Wei, Ulf Garbe, Dehong Yu, Brunet Edouard, Aihong Liu, Jun Ding, *Robocasting of dense yttria-stabilized zirconia structures,* Journal of Materials Science 53 (2018) 247-273.

On this article, aqueous ceramic suspension comprising nano-sized yttria-stabilized zirconia (YSZ) powder has been developed for robocasting purpose. Both fully and partially stabilized zirconia. A further microstructural and mechanical characterisation of the printed parts has been done, demonstrating that aqueous-based ceramic suspension is suitable for the fabrication of large YSZ parts with good repeatability.

This article covers one of the goals of this master's thesis; the microstructural mechanical characterisation of fully stabilized zirconia (cubic phase) produced by means of robocasting technique. Although in this article they have used a 6 %mol. yttria content and 0.25 wt% Al_2O_3 to obtain fully stabilized zirconia phase, the final microstructural properties should be similar, or almost the same, as the powder used for the present thesis.

It has been studied the density of the printed parts, achieving > 94% of the theoretical density, and the shrinkage of the green bodies compared to the sintered part and the original CAD design. It has been stated that the parts present and anisotropic shrinkage depending on the axe-direction. The green parts have been sintered at different temperatures; 1450, 1500, 1550, 1600 and 1700 °C, achieving the greatest density at 1600 °C. Finally, a study of the grain size of the printed samples was done using SEM images.

A. Ghazanfari, W. Li, M.C. Leu, J.L. Watts, G.E. Hilmas, Additive manufacturing and mechanical characterization of high density fully stabilized zirconia, Ceramics International 43 (2017), 6082-6088.

In this article, the mechanical properties of additively manufactured 8 % mol. yttria-stabilized zirconia (8Y-TZP) parts were extensively studied. A novel freeform extrusion fabrication process, called Ceramic On-Demand Extrusion (CODE), was employed to deposit an aqueous viscous suspension (50 vol% solids loading) of fully stabilized zirconia powder in a layer-by-layer fashion. the parts were humid-dried in an environmental chamber and densified by sintering under atmospheric pressure. Standard test methods were employed to examine the properties of sintered parts including density, Vickers hardness, fracture toughness, Young's modulus, and flexural strength. Microstructural evaluation was also performed to observe the microstructural morphology and measure grain size. The results indicate that the properties of 8YSZ parts produced by the CODE process match those obtained by conventional fabrication techniques, in this case, cold isostatic press (CIP).

This article covers all the aspects in reference to the mechanical properties that this Master's thesis will study. Although, they do not use the same additive manufacturing technique, they do use the same powder from Tosoh.

They analyse the drying process, the sintering process, the shrinkage of the samples and the mechanical properties, comparing them to traditional manufactured samples via CIP.

It will be of a great importance when comparing it to the results found in this Master's thesis.

J. J. Roa, J. C. Ruiz-Morales, J. Canales-Vàzquez, M. Morales, X. G. Capdevila, P. Núñez, M. Segarra, Mechanical Characterisation at Nanometric Scale of New Design of SOFCs, Fuel Cells 11 (2011), No. 1 124-130.

On this paper the mechanical properties, Hardness and Young's modulus, of SOFCs based on YSZ and NiO-YSZ composites, have been studied. They obtained that the elastic-to-plastic transition occurred at 25 nm of penetration depth using Berkovich indenter. Also, they obtained the followings values of Young modulus; for YSZ 260 ± 15 GPa and for NiO-YSZ 205 ± 20 GPa. This micromechanical property was reported for the first time in this manuscript.

All these values will be so useful to compare with the values that will be obtained at the micrometric length scale during this master's project for the different electrolytes manufactured by AM technique used for SOFCs applications will.

Luyang Wei, Jinjin Zhang, Fangyong Yu, Weimin Zhang, Xiuxia Meng, Naitao Yang, Shaomin Liu, *A novel fabrication of yttria-satbilized-zirconia dense electrolyte for solid oxide fuel cells by 3D printing technique,* International Journal of Hydrogen Energy (2019).

This article is focused on dense 8 %mol. yttria-stabilized-zirconia (8YSZ) electrolyte fabrication via digital light processing (DLP)-stereolithography-based 3D printing technique. The density of the sintered electrolyte was measured as 99.96 % by Archimedes' water displacement method. It also studies the fabrication of a full cell, fabricated of silver- $Ce_{0.8}Gd_{0.2}O_{1.9}$ (Ag-GDC) as cathode/anode, and its electrical properties.

Loïc Ferrage, Ghislaine Bertrand, Pascal Lenormand, *Dense yttria-stabilized zirconia obtained by direct selective laser sintering,* Additive Manufacturing 21 (2018) 472-478.

This article focusses also on a different 3D printing technique called selective laser sintering (SLS), which uses a laser beam as a power source to selectively sinter or melt a powder bed. They use 8 mol% yttria-stabilized zirconia powder from Tosoh, the same powder that will be used in this project. The study of the particle size and distribution has a great importance in order to compare to. In addition, the study of the microstructure and the crystalline phases are of great importance.

2. Goal

The goal of this Master's thesis is to characterize, microstructurally and mechanically, 8 %mol. yttria stabilized zirconia which is used for solid oxide fuel cells (SOFC) electrolytes. In order to do so, a comparison between conventional processing routes and robocasting technique, additive manufacturing technique, is going to be carried. This is a relatively new zirconia material used for this application and this research aims to reassert its use along with additive manufacturing processing routes.

The main job of this research is divided in four different parts:

i. To manufacture fully dense samples using CIP process (used as reference) and to print SOFCs electrolytes with different tubular geometries.
ii. To evaluate the microstructural and mechanical properties for both specimens.
iii. Study the effect of the drying conditions on the final properties of the 3D printed samples.
iv. Study the main defectology induced during the 3D printing process in order to be able to detail the main 3D printing drawbacks.

In general terms, the main scope of this research is to evaluate the reliability of robocasting 3D printing technique, in terms of mechanical and microstructural properties, to manufacture tubular zirconia SOFCs electrolytes.

3. Experimental procedure

3.1. Materials

On this section the two main materials employed to produce the detailed gelling agent and the ceramic paste will be explained. Pluronic F-127 was used as polymeric matrix and gelling agent (Pluronic F-127® from *Sigma Aldrich (**Annex A.1**: Pluronic F-127 Sigma Aldrich)*), and 8 mol% yttria-stabilized zirconia powder from Tosoh (***Annex A.2***: Zirconia powder from Tosoh).

3.1.1. Pluronic F-127®

The Pluronic F-127® from *Sigma Aldrich* is a copolymer used to produce hydrogels, mainly for medical applications.

Pluronic F-127® [18] are amphylic copolymers comprised of two external blocks of polyethylene oxide (PEO) and a central block of polypropylene oxide (PPO), comprising a global formula (PEO-PPO-PEO) and a nominal molecular weight (M_n) of 12,500 [19], as it is shown in ***Figure 3.1.*** These copolymers present a thermal inverse mechanical behaviour in aqueous dissolution due to the gelling process that they suffer with temperature; in particular when the temperature increases. This behaviour is mainly originated by the difference in the critical dissolution temperature between the PEO and the PPO. The gelling temperature and mechanical strength of the gel depends on the concentration of polymer and the chain length of PEO and PPO.

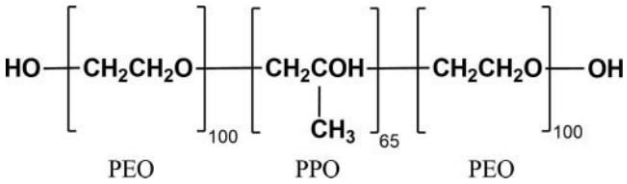

Figure 3.1. *Structural formula of P127 block copolymer [20].*

In this master's thesis, Pluronic F-127® is used to create an hydrogel with distilled water. The behaviour of the obtained solution, depending on the concentration of copolymer used, will exhibit a liquid behaviour below the sol-gel transition temperature (Tg), which is comprised between 20 - 30 ^{o}C [21]. Over this temperature, the shear/viscosity module ratio will increase by several orders of magnitude in a narrow range of temperatures. This point must be considered because the concentration in water will affect the porosity created during the sintering process. Thus, it could cause the failure of the material.

The hydrogel used in this project will be composed of a 25%wt of Pluronic F-127® and a 75%wt of distilled water which is approximately equivalent to 30%w/v. Hence, according to ***Figure 3.2***, the gelation point will be close to 14°C. Therefore, the hydrogel will have a liquid state once put in a fridge and recover its gelling state at room temperature for printing.

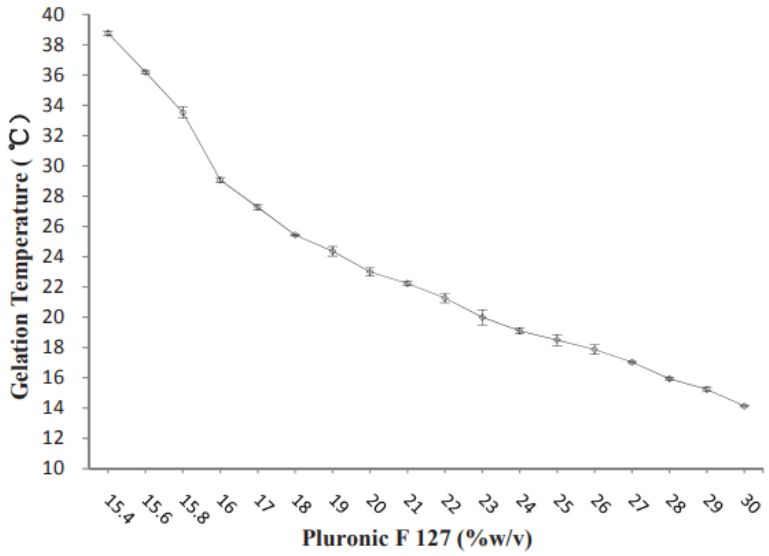

Figure 3.2. *Gelation temperature and thermoreversible behaviour of P127 [18].*

3.1.2. Zirconia powder

In this Master's thesis, the 8 %mol yttria-stabilized zirconia (8Y-ZTP) will be employed to manufacture the electrolyte of SOFCs. The 8Y-ZTP powder is supplied by Tosoh (***Annex A.2***: Zirconia powder from Tosoh*)* and it does not contain any binder and will therefore be considered as pure 8 mol% yttria-stabilized zirconia. For more information about the properties and crystallography of zirconia see **section 1.3.1.1**.

The same powder will be used to manufacture the samples by cold isostatic pressing (CIP) and to prepare the ceramic paste to print the SOFC electrolyte.

3.2. Ceramic paste preparation

In this section, two different things will be explained in detail: *(i)* the preparation procedure as well as *(ii)* the composition of the ceramic paste that will be employed to manufacture the electrolyte. The paste consists on a mixture of three different materials: distilled water, the gelling agent (Pluronic F-127®, see ***section 3.1.1)*** and 8Y-ZTP powder *(see* ***section 3.1.2*** and ***Annex A.2***: Zirconia powder from Tosoh for more information).

To prepare the mixture, the compositions are based on the different studies conducted in CIEFMA's research group, more information can be found in [19, 20].

In order to obtain the printing ceramic paste is important to consider the following steps:

(i) Preparation of the hydrogel, which consists on a mixture between polymeric material (Pluronic F-127®) and distilled water.

(ii) Mixing the hydrogel with the desired ceramic powder to obtain the final paste that will be used to print.

The preparation of the hydrogel consists on mixing the Pluronic F-127® with distilled water with the help of a SpeedMixer (*CosSearch GmbH*), presented in ***Figure 3.3***. The proportion used will be 25 wt% of copolymer and 75 wt% of distilled water. In order to prepare 100 g of hydrogel the following steps were followed:

1) Weight and mix in the SpeedMixer during 5 min at 3500 rpm 25 g of distilled water and 25 g of P127 at ambient temperature.
2) If needed, break the mixture obtained in the previous step with a spatula in order to maximize the mixing process.
3) Weight and add 50 g of distilled water and mix during 5min at 3500 rpm, in order to get the desired composition.
4) Store the final mixture at a constant temperature inferior to the gel/sol transition during 24 h (for instance in a fridge at 4 ^{o}C, to accelerate the process) in order to eliminate the residual bubbles generated during the mixing process. This step is used in order to avoid any subsequent printing defects induced during the preparation of the ceramic paste.

Figure 3.3. *SpeedMixer used to mix the hydrogel and ceramic paste.*

Since the hydrogel is prepared, it is possible to start the ceramic paste preparation. According to the previous studies conducted in CIEFMA's research group to print SOFC electrolytes, the optimal composition of the ceramic paste was determined as: 70 wt% of ceramic powder and 25 wt% of hydrogel.

The ceramic paste fabrication is realized following the next steps:

1) Weight and mix during 1 min at 3500 rpm the total amount of ceramic powder and hydrogel needed.
2) If needed, mix the ceramic paste with a spatula in order to homogenize the mixture and mix again in the SpeedMixer with the same conditions explained in step 1). This process may be repeated until a homogeneous mixture is obtained.
3) Let the obtained paste rests for 2 h before print in a control humidity atmosphere (HR ≈ 95 %) to avoid water evaporation.

3.3. Characterization of the ceramic paste

The robocasting technique consists on extruding a viscous liquid, or in this case a ceramic paste, through a nozzle, as explained before in ***section 1.4.2***. So, it is important to characterise the fluid that is going to be used to print, in order to achieve the desired properties that will meet with the printing geometries, nozzle diameter, extrusion load, and other parameters involved in this AM technique.

To do so, along ***sections 3.3.1*** and ***3.3.2***, an exhaustive study of the particle size of the powder and a rheology study of the hydrogel and the ceramic paste is detailed.

3.3.1. Particle size

To measure the particle size of the ceramic powder, which will determine what nozzle diameter will be used, it has been used the *Mastersizer 3000*, see ***Figure 3.4***. It uses the technique of laser diffraction to measure the size of particles. It does this by measuring the intensity of light scattered as a laser beam passes through a dispersed particulate sample. Through this technique, it is possible to analyse both wet and dry dispersions in a range between nanometres to millimetres particle sizes [24].

Figure 3.4. *Mastersizer 3000 used during this Master's thesis.*

Once the experiment is done, a diffraction pattern is obtained where the size of the particle is plotted against the volumetric percentage amount (of this particle size) present in the powder.

3.3.2. Rheology: Determination of the gel point

In this Master's thesis, an important parameter is the determination of the sol-gel point of the Pluronic F-127, used as hydrogel for the ceramic paste. In order to experimentally determine the sol-gel point a rotational (or oscillatory) rheology test has been done.

Oscillatory rheology

The basic principle of an oscillatory rheometer is to induce a sinusoidal shear deformation in the sample and measure the resultant stress response. In a typical experiment, the sample (in this case the hydrogel and the ceramic paste) is placed between two plates, as shown in ***Figure 3.5***. While the top plate remains stationary, a motor rotates the bottom plate imposing a time dependent strain on the sample. In this case, the experiment was done at constant temperature of T = 25 ^{o}C and frequency ω = 1 Hz.

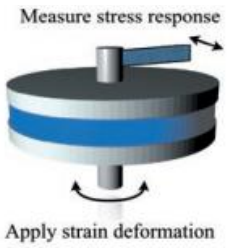

Figure 3.5. *Schematic representation of a typical rheometry setup* [25].

In a typical rheological experiment, it seeks to measure G'(ω) and G''(ω), where G' is the storage or elastic modulus, and the G'' is the loss or plastic modulus, which respectively characterise the solid-like and fluid-like contributions to the measured stress response.

According to [26], the gelation of a cross-linking polymer is correlated with the crossover of the dynamic storage *G'* and dynamic loss *G''* modulus, allowing to easily determine the sol-gel point of the hydrogel and ceramic paste used in Master's thesis.

The equipment used for this experiment is a *RheolabQC* rheometer. It has a temperature sensor that allows to control the temperature of the test and equals to room temperature, 25 ºC.

3.4. Additive manufacturing process

Robocasting technique will be used during this master's thesis as an AM process to print the 8Y-ZTP electrolyte parts. The model of the machine is a RepRap BCN 3D+ printer with dual paste head, see ***Figure 3.6***, supplied by the "Fundació centre CIM-Technical University of Polytechnic-BarcelonaTech". The use of different software was required in order to obtain the final 3D-model of the part and the readable code for the 3D printer.

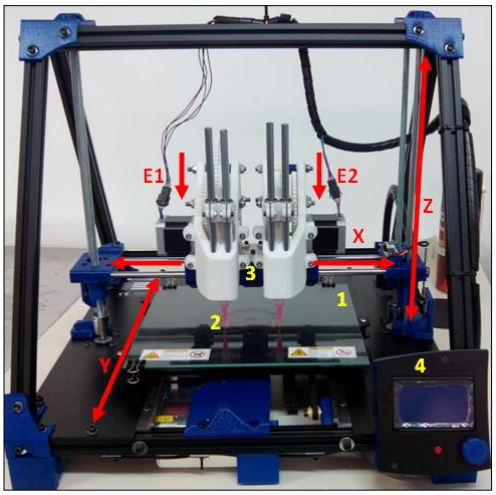

***Figure 3.6**. RepRap BCN 3D+ printer used during the project* [27].

The 3D printer allows 3-axis direction (X, Y, Z) movements. The head ensures the movements in *X*- and *Z*- axis, while the printing bed ensures the *Y*-direction. The complete system consists of the following parts (the different numbers explained below correspond with the different numbers located in ***Figure 3.6***:

1. Printing bed: The place where sample is printed. To minimise the adhesion of the sample to the bed, cellulose filter paper or parafilm was used.
2. Printing syringe: It acts as a printing extruder and is the part where the ceramic paste is loaded.
3. Printing heads: These are made of two parts:
   - *Base*: Attached to the printer frame. It consists of an eight-gear train that applies the force to printing piston. The syringe fits into a hole drilled in this base.

- *Piston*: It is coupled to the gear train by a toothed face and to the syringe by a male-female system. It is responsible for converting the rotational movement of the gears into uniaxial printing force on the ceramic paste.

4. Control knob: From where the printer functions are controlled. It contains a SD slot to load the *gcode* files.

3.4.1. Modeling

The 3D-modeling of the part was done on FreeCad (see ***Annex B.3***: FreeCad), a free Computer Assisted Design (CAD) software. A tubular geometry (see ***Figure 3.7***), with different diameter ratios, have been modelled in order to mechanically and microstructurally characterize. Cylindrical samples (see ***Figure 3.7***) have also been modelled to study the elastic modulus as a function of the residual porosity size and form factor, in order to enhance the final density of the printed electrolyte.

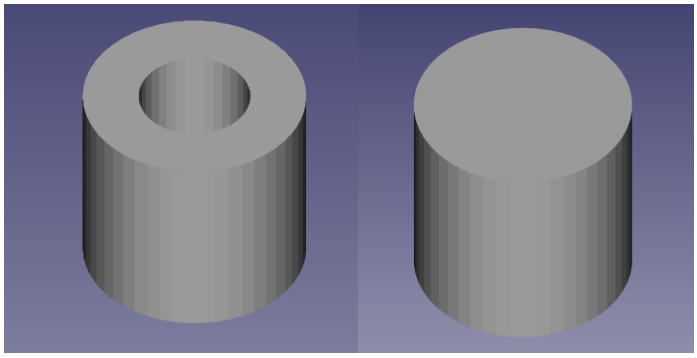

Figure 3.7*. Schematic representation of the tubular and cylindrical geometries created with CAD design.*

3.4.2. Printing conditions

Once the part is designed, it can be saved as a "*.stl"* file format, which can be used by the next software, *Slic3r*, see ***Annex B.1***: Slic3r. This software allows the user to generate a *gcode* file that will be read by the printer. To do so, this software divides the solid part in thin layers depending on the conditions entered by the user, such as; the position on the printing bed, what kind of infill will be used for each layer, the infill percentage to control the density of layers, the printing speed and the non-printing movements speed among others. It also takes into account the syringe diameter and the tip diameter used. For a correct filament diameter while printing, a 0.58 mm diameter *Nordson EFD Optimum® Systems* nozzle was used, more information can be found in ***Annex A.3***: *Nordson EFD Optimum® Systems* nozzle.

During the printing process in this Master's thesis, the following conditions were employed, see ***Table 3.1***:

Table 3.1. *Summary of the printing process conditions.*

SOFC electrolyte geometry	Infill (%)	Pattern	Speed for printing moves (mm/s)						Layer height (mm)	Nozzle diameter (mm)
			Perimeters	*Small perimeter*	*Infill*	*Solid Infill*	*Bridges*	*Gap infill*		
Tubular	100	rectilinear	10	10	5	5	10	20	0.522	0.58

In ***Figure 3.8***, it can be seen a representation of the different infill percentages and infill pattern that can be used while printing.

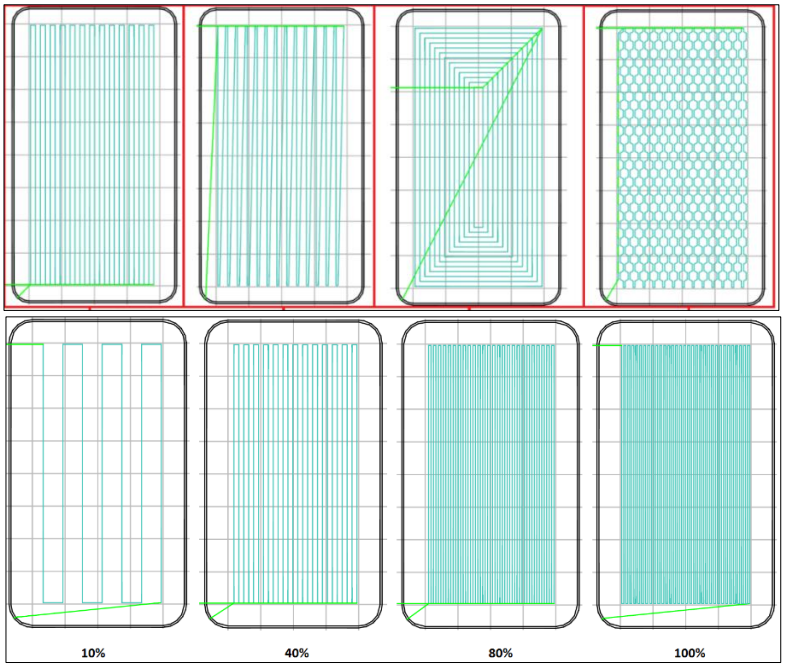

Figure 3.8. *Schematic representation of infill percentages and infill patterns* [27].

3.4.3. Working conditions

The AM process has been done at the laboratory conditions as summarized below:

- ***Temperature:*** 20ºC
- ***Humidity:*** *70 %*
- ***Pressure:*** 1 atm

Before starting to print is important to temperate the ceramic paste. Increasing the temperature helps to get the correct printing viscosity and avoids that the paste might precipitate before the process. There are different ways to do that (like heating the mixture in a bain-marie), but the way it was done in this Master's thesis was to introduce the mixture in the SpeedMixer during 1 min.

3.5. Cold isostatic pressing

Cold isostatic pressing (CIP) was used in this Master's thesis as a traditional processing technique to manufacture ceramic samples, which will be used as a reference. First step is to prepare 3 g of 8Y-ZTP and introduce it into the pressing chamber. An 8bar pressure for 30 seconds is applied to obtain a green body. Afterwards, the green body is introduced in a latex glove and with the help of the *BUCHI Vacuum Pump V-100,* vacuum is applied into the glove for a better pressure distribution. Secondly, the glove with the sample is introduced into the pressing chamber, full of machine oil, to apply a hydrostatic pressing to the sample. To do so, a 25 bar pressure during 2 min is applied. Finally, the sample is fully compressed and ready to be sintered.

The CIP process was conducted by means of an *MTI Corporation CIP YLJ-20TA* machine, see ***Figure 3.9***, was used.

Figure 3.9. *MTI Corporation CIP YLJ-20TA.*

3.6. Sintering process

This step becomes relevant during the process of the final specimen obtention. In this type of manufacturing process, the parts cannot be compacted due to the complex shapes and/or geometries. Within this context, the sintering process is a key step in order to densify the green bodies and reach the desired microstructure and mechanical properties. The sintering process of the different specimens was made on a *Nabethern* furnace, see ***Figure 3.10***.

***Figure 3.10**. Nabathern furnace used to sinter the samples.*

According to previous [22], [23], the optimal thermal treatment to obtain the maximum density and therefore, the best mechanical properties, is detailed in ***Table 3.2*** and represented in ***Figure 3.11***. In addition, the thermal treatment to reveal the grain, which is important to study the microstructure of the samples, is detailed also in ***Table 3.2***.

***Table 3.2.** Summary of the T.T conditions for each treatment.*

T.T.	Sintering treatment	Grain revealing
1st heating time	4h	4h
1st stop	700ºC – 1h	700ºC – 1h
2nd heating speed	4h	4h
2nd stop	1450ºC – 2h	1300ºC – 2h
Cooling down speed	8h	8h

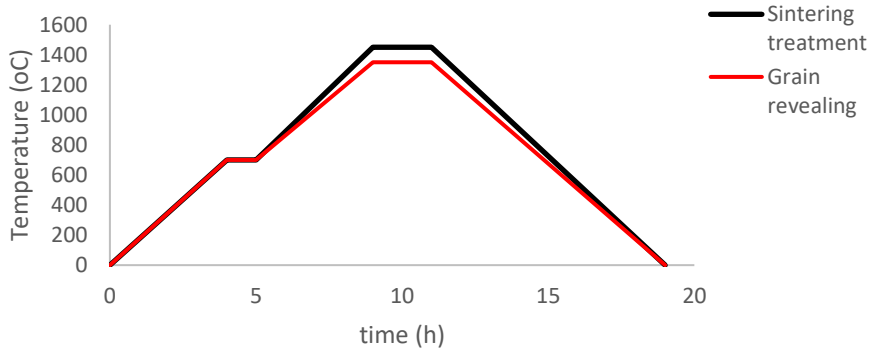

Figure 3.11. *Representation of the thermal treatment for the sintering process (black) and revealing microstructure (red).*

3.7. Polishing process

The polishing process is an experimental procedure, usually done in materials science, prior to the mechanical and microstructural characterization of metallic and ceramic materials. This process is required in order to smoothen the surface which is required, in further steps, to be able to analyse the samples with the following techniques: optical microscope, scanning electron microscopy (SEM), X-Ray diffraction (XRD), laser confocal microscope and many other advanced characterization techniques.

Two main goals need to be reached during this process: planarity of the specimen and a mirror like surface. To do so, a prior preparation of the samples need to be done. In order to get the desired planarity, the specimens were embedded in Bakelite and/or epoxy resin. Due to the elevated pressure involved in the process of embedding the sample in Bakelite, some samples were destroyed, as seen in ***Figure 3.12***. Therefore, it was used an epoxy resin.

Figure 3.12. *Destroyed embedded sample in Bakelite.*

The next step was the polishing process itself. It was done in a manual polishing machine from *Struers (LAboPol-5)*, see ***Figure 3.13.a.*** Different grain size polishing papers and different suspension were used (see ***Figure 3.13.b***). All the information related on the polishing process is summarized in ***Table 3.3***.

Table 3.3. *Summary of the different parameters employed during the polishing process.*

Step	1	2	3	4	5	6	7
V (rpm)	200	200	200	200	200	200	200
Polishing paper	Sandpaper P:120	Sandpaper P:320	Sandpaper P:600	Sandpaper P:1200	Polishing cloth	Polishing cloth	Polishing cloth
Suspension	Water	Water	Water	Water	6 µm	3 µm	SiO_2 colloidal

Figure 3.13. *a) Polishing machine and b) polishing clothes and suspensions used during the polishing process.*

3.8. Characterisation techniques

In this section, the main techniques employed to microstructurally and mechanically characterise the ceramic samples are briefly explained.

3.8.1. Density

The study of the density is decisive for the results analysis; it gives a qualitative idea of the percentage of internal porosity as well as a parameter to compare the quality of the 3D printed specimens and the specimens manufactured by CIP.

As it has been explained in the Introduction section, the SOFC's electrolytes must be dense. Due to these requirements, all samples may acquire a relative density higher than 90%. In this sense, the specimens with a relative density lower than the presented threshold will be excluded.

The density (ρ) of the samples has been determined by the Archimedes method. Archimedes' principle states that the upward up thrust exerted on a body immersed in a fluid, is equal to the weight of the fluid that the body displaces. Firstly, the sample is weighted in air followed by submerging it in the fluid. Then, using ***equation 3.1***, the density value can be determined.

$$\boldsymbol{\rho = \frac{A}{A - B}(\rho_0 - \rho_L) + \rho_L} \qquad \textbf{(Eq. 3.1)}$$

Where *A* and *B* represent the weight of the sample in air and in the fluid employed (distilled water), respectively. With $\rho_{\mathbf{0}} = 1\ {}^{g}/_{cm^3}$ (density of the fluid) and $\rho_L = 0.0012\ {}^{g}/_{cm^3}$ (density of air).

All measures were made in a balance from *Mettler Toledo*, model xs3035 as depicted in ***Figure 3.14***. The different parts of the balance are described below:

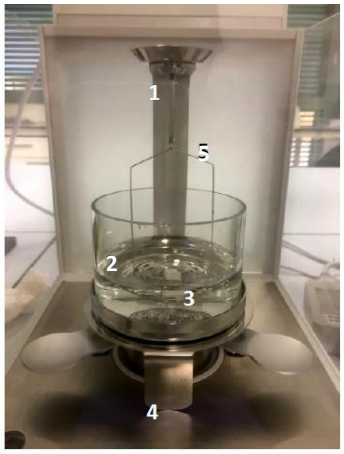

Figure 3.14. *Archimedes' method set-up in Mettler Toledo balance.*

1. Platform to locate the sample to calculate its weight in air.
2. Recipient to fill the fluid (distilled water) to submerge it.
3. Platform to locate the sample to calculate its weight in water.
4. Recipient's support.
5. Support to submerge the sample.

Furthermore, the environmental conditions employed during the test, must be taken into consideration:

- **Temperature:** 18.2ºC.
- **Auxiliary fluid:** distilled water.
- **Principal fluid:** air.
- **Relative humidity:** 31 %.

3.8.2. Magnifying glass

Due to the importance of the geometry, the final dimensions of the samples were calculated to see the contraction after the sintering process. In this sense, a magnifying glass was used.

The magnifying glass used during the Master's thesis was an *Olympus SZX16*, see ***Figure 3.15***. To study the samples different lens were used:

- **x0.7:** To big geometries like the external diameter of the tubular samples.
- **x0.8:** More specific zone like the internal diameter of the tubular samples and the superficial defects.

Figure 3.15. *Magnifying glass used during this Master's thesis.*

3.8.3. Optical microscope

An optical microscope (OM) uses visible light and a system of lenses to magnify images, an scheme of this device is depicted in ***Figure 3.11***. It will be used to check the surface porosity and defects of the different printed samples.

The OM used during this Master's thesis was an *Olympus BX53m* microscope, see ***Figure 3.16.*** This microscope is equipped with different magnifying lenses, but the most used in this work were the following ones:

- **x10:** To have a general view of the superficial state of the samples.
- **x20:** To magnify a specific defect or porosity to study the geometry of them.

Figure 3.16. *OM used during this Master's thesis.*

3.8.4. X-Ray diffraction

X-Ray diffraction (XRD) technique consists on a beam of electrons accelerated, that impacts to a target material, producing the interaction between the electrons and the material.

All crystalline solids consist of a regular array of atoms, ions or molecules with interatomic spacing on the order of 100 pm or 1 Ä. There will be a part of the incident beam that will be absorbed by the material and the other one will be reflected. This reflected part is the beam that the machine defects in a wavelength. For each material and different phase that exists, there is a wavelength associated to it.

An XRD equipped with a PIXcel3D detector was used, see ***Figure 3.17***, to record the XRD patterns of the crystallography phases present on both 8Y-TZP samples, CIP and 3D printed, used during this Master's thesis.

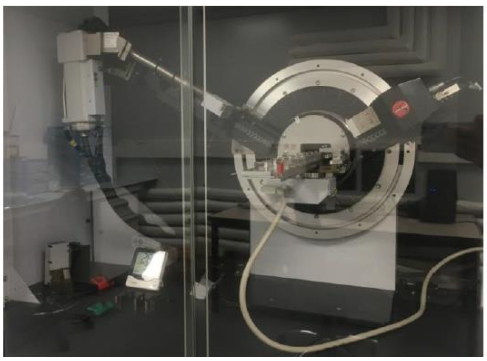

Figure 3.17. *XRD equipment used during this Master's thesis.*

The different spectrums were recorded by using the following conditions:

- ***Step size:*** 0.02º
- ***2θ range:*** 20 to 90º

3.8.5. Field Emission Scanning Electron Microscope

Field Emission Scanning Electron Microscope (FESEM) is a Scanning Electron Microscope (SEM) based technique. SEM uses a focused high-energy electron beam to generate a variety of signals at the surface of the solid specimen. The image is formed by a scanning the sample and collects the signals that derive from the electron-sample interactions. Theses interactions reveal important microstructural information like texture, chemical composition, crystalline structure and orientation of materials. FESEM also employs a beam of highly energetic electrons and the concept field appears by the generation of an electric field, because the surface of the samples is conductor. In this sense, the non-conductive specimens may be coated by a conductive material, like carbon. For this process, the equipment requires an extreme vacuum in the column of the microscope (around 10^{-6} Pa). FESEM involves an electron emission cathode and anodes, see ***Figure 3.18.a.*** The acceleration voltage between these electrodes is commonly in the range of 0.5 to 30 kV.

An electron detector perceived the secondary electrons (SE) emitted, and the image is created by comparing the intensity of SE to the scanning primary electron beam. The ***Figure 3.18.b*** shows the model of FESEM used during this Master's thesis.

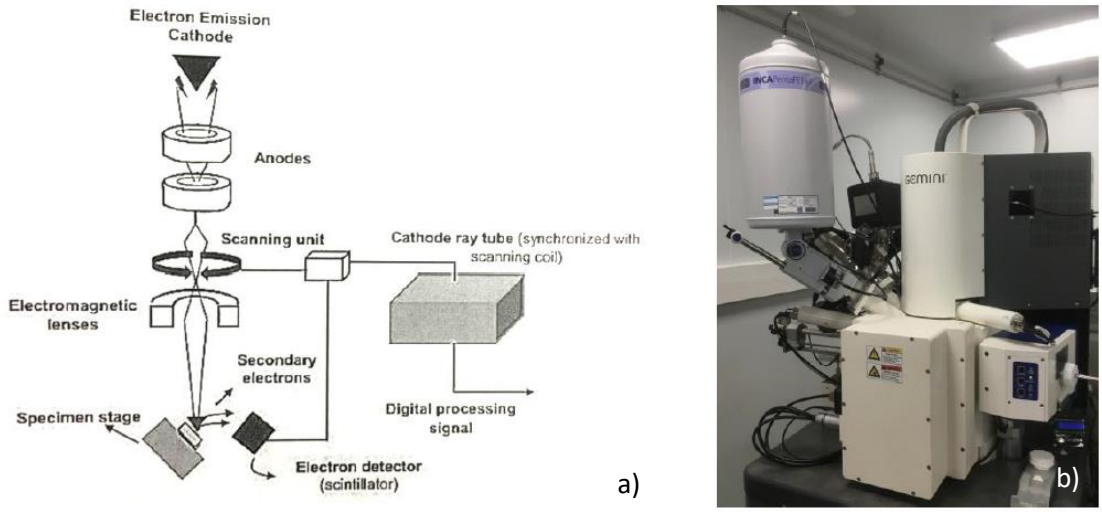

Figure 3.18. *a) FESEM schematic representation* [28]*, and b) FESEM model used during the Master's thesis.*

In this master's thesis the FESEM was used to study the superficial porosity, the grain size and to observe the damage induced by the indentations generated onto the samples.

3.9. Mechanical characterization techniques

3.9.1. Micro indentation: Vickers indentation

Hardness (*H*) has been defined as "material's resistance to plastic deformation". The term *H* may also refer to resistance to bending, scratching, abrasion or cutting. The usual method to achieve a *H* value is to measure the depth or area of an indentation left by an indenter of specific shape, with a specific force (*F*) for a specific time.

The Vickers hardness (*HV*) test method consists of indenting the test material with a diamond indenter, in the form of a right pyramid (see ***Figure 3.19.a***) with a square base subjected to a load of 1 to 100 kgf (kilogram force). The indenter is in contact at the desired load for 10 to 15 seconds. The two diagonals of the indentation left in the surface of the material are measured using a MO.

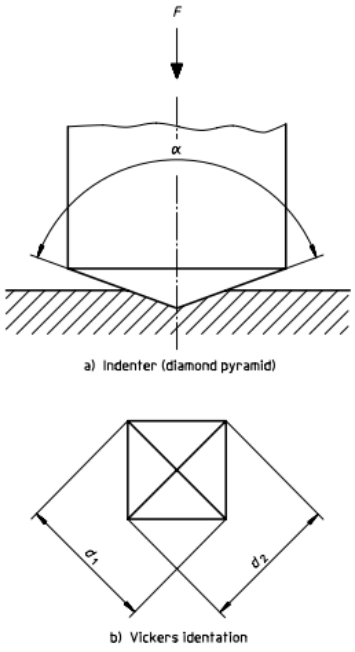

Figure 3.19. *a) Indenter diamond pyramid, and b) Representation of the diagonals of the indentation* [29].

The hardness of the material corresponds of the ratio *F* divided by area (*A*), where *F* is the load applied by the machine (N) and *A* is the sloping area of the indentation (mm^2). Therefore, Vickers hardness (*HV*) can be calculated using the **Eq.3.2**:

$$HV = 0.1891\frac{F}{d^2} \qquad \textbf{(Eq. 3.2)}$$

where *F* is the force applied (N) and *d* the mean size of the diagonals (mm) (***Figure 3.19.b***). Therefore, *HV* is directly expressed in MPa.

To perform the test, it must be taken into consideration that the plastic properties of the material undergo local modification during the indentation. Thus, each indentation must be spaced from the precedent ones, at least 10 times the maximum penetration depth. For each sample, CIP and AM specimens, five imprints per load (at 10 and 1 kgf), respectively, were done using the *EMCO-TEST Durascan* equipment, see ***Figure 3.20***, in order to provide a representative *HV* value with statistical signification.

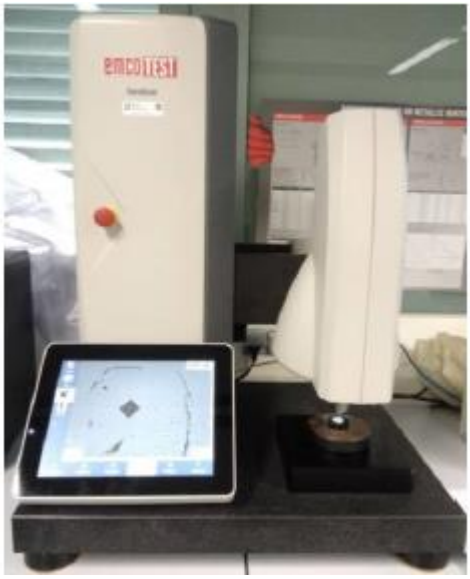

Figure 3.20. *Vickers hardness machine EMCO-TEST Durascan.*

3.9.2. Nanoindentation

This technique is like the micro indentation technique explained before. The results of this test are dependent on the scale and the test method. So, depending on the characteristics of the indentation and the strain field, mechanical testing methods can be classified as macro-, micro-, nano- and pico-indentations.

In this case, the nanoindentations were applied in order to determine the mechanical properties (hardness and elastic modulus) with a Berkovich indentation tip (see ***Figure 3.21***) at penetration depths lower than 2000 nm.

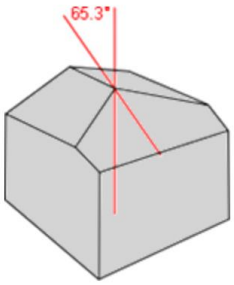

Figure 3.21. *Berkovich tip* [30].

As it can be seen in ***Figure 3.21***, the Berkovich tip is a three-sided pyramid. The angle between the centreline and the three faces is 65.3º. The three-face design allows grinding the tip to a sharp point. It is suitable for bulk materials, thin films, polymers, scratch testing and wear testing [30].

In this Master's thesis the Berkovich tip was used in order to measure the hardness (*H*) and the elastic modulus (*E*) at the submicrometric length scale.

Hardness (*H*) and elastic modulus (*E*) are the most measured properties as a function of the displacement into the surface (*h*) determined during a nano-indentation essay. The method of Oliver and Pharr is used to directly determine the micromechanical properties through the loading-unloading or *P-h* curve (see ***Figure 3.22***). This methodology allows determining on a direct way both mechanical properties. This method can obtain these information thanks of the data obtained during one cycle of loading and unloading, from an indentation of the material.

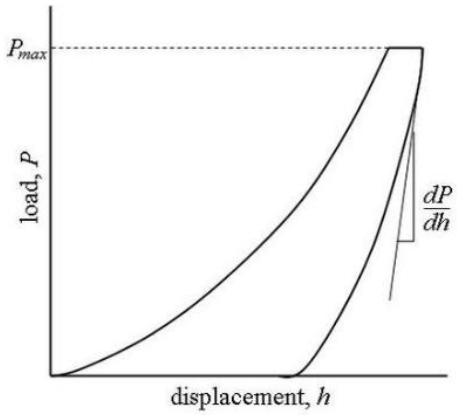

Figure 3.22. *Schematic P-h curve* [31].

In particular, to get the values of these properties the procedure is based on the unloading process shown schematically in ***Figure 3.23***, in which it is assumed that the behaviour of the Berkovich indenter can be modelled by a conical indenter [32].

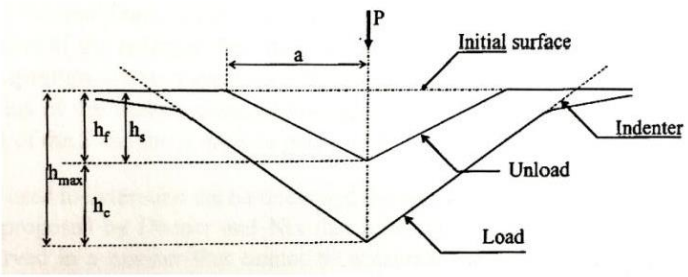

Figure 3.23. *Schematic illustration of the unloading process showing parameters characterizing the contact geometry* [33].

There are three main conditions that you can control: the number of indentations per test, the distance between each indentation and the depth of the print. These two lasts ones are important. During an indentation essay, the print that generates the tip has a zone with an elastic deformation and when the applied stress is higher than the yield strength of the material the plastic deformation zone appears. The elastic deformation zone is near 20 times the maximum displacement into the surface (h_{max}), while the plastic zone has a rate of 7 to 10 times the h_{max}. For this reason, to avoid the influence of the plastic zone to other indentation and slightly modify the hardness value, the distance between imprints at least may be keep constant and equals to 7-10 times the displacement into surface.

To attempt and evaluate the composite hardness and elastic modulus for the different specimens investigated here, a homogeneous array of 36 imprints (6 by 6) was performed by using the Berkovich indenter. This array was performed at 2000 nm of maximum displacement into surface or until reaching a maximum applied load of 650 mN by using a nano indenter XP (MTS, see ***Figure 3.24***) equipped with a continuous stiffness measurement (CSM) module, the later allowing a dynamic determination of the mechanical properties during the indentation process. A constant distance around 50 µm was held constant between each imprint in order to avoid any overlapping effect. Along the indentation process, the indentation strain rate was held at 0.05 s^{-1}.

Figure 3.24. *Nano indenter set-up used during this Master's thesis.*

3.9.3. Micro-compression test

For uniaxial tests, the velocity of compression is typically held at constant rate, and the displacement and resulting load are recorded. The load is measured by a series of strain gages, or "load cell", while the displacement can be recorded as displacement of the crosshead, or the beam on which the specimen load frame is mounted. To make direct comparisons between materials, loading responses must be normalized against sample geometry. Therefore, the dimensions of each sample are noted to compute stress and strain from load and displacement, respectively [34].

Then, a compression stress-strain (σ–ε) curve can be generated from the recorded load and displacement. A typical stress-strain profile for the different elastic-plastic behaviour of materials resembles the following (see ***Figure 3.25***):

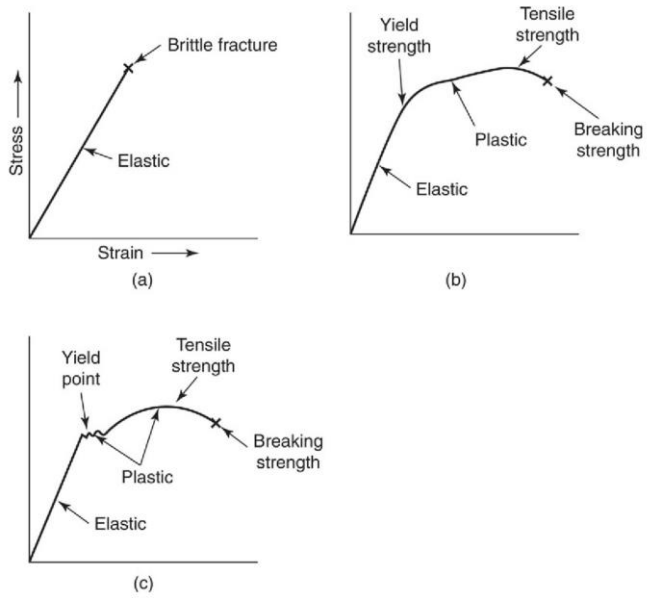

Figure 3.25. *Types of stress-strain behaviour* [35].

In this Master's thesis, a compressive strength test was conducted in order to mechanically test the samples manufactured via 3D printing. To do so, a *ToniVERSAL* press from *Toni Technik* was used (see ***Figure 3.26***). The test was done following the *UNE-196* norm, which stablishes the methods and parameters for testing cement. Due to the dimensions of the samples, some parameters were modified, like the load rate applied (0.01 kN/s).

Figure 3.26. *ToniVERSAL press used during this Master's thesis.*

4. Results and discussion

4.1. Density

Three different groups of samples have been done depending on the drying time before the sintering process. The two different geometries that have been printed are cylindrical and tubular, the lasts ones with different internal diameters of 3, 4 and 5mm (labelled as D3, D4 and *D5,* respectively, along this section). The CIP sample, taken as reference, has a $\rho_{CIP} = 5.95$ kg/m^3. The relative humidity (% HR) was held constant sand equals to 85% for the Group A and B specimens while for the group C was held constant to 65 % in order to observe if the HR can be considered as a key parameter in the 3D printing process.

In the ***Group A*** (see ***Table 4.1***)*,* twelve samples with different geometries were printed. They were dried for a total period of 6h.

Table 4.1. *Summary of the density results of samples from Group A.*

Type	Sample	ρ (kg/m^3)	ρ / ρ_{CIP} (%)
Cylindrical	3	5.77 ± 0.09	96.9
D3	3	5.81 ± 0.02	97.7
D4	3	-	-
D5	3	5.70 ± 0.11	95.8

In the ***Group B*** (see ***Table 4.2***)*,* six samples with the same geometry were printed. They were dried for a total period of 2 days.

Table 4.2. *Summary of the density results of samples from Group B.*

Type	Sample	ρ (kg/m^3)	ρ / ρ_{CIP} (%)
Cylindrical	7	5.82 ± 0.08	97.8

In the ***Group C*** (see ***Table 4.3***)*,* twelve samples with the same geometry were printed. They were dried for a total period of 17 days.

Table 4.3. *Summary of the density results of samples from Group C.*

Type	Sample	ρ (kg/m^3)	ρ / ρ_{CIP} (%)
Cylindrical	3	5.79 ± 0.02	97.3

It is necessary to mention that the density of D4 and D5 samples was not able to be determined due to during the sintering process, the specimens broke, mainly due to printing defects that appeared on the samples' walls, that were not able to withstand the thermal treatment (TT). Hence, it was decided to not print more tubular samples.

The final density of the samples is mainly related to the porosity and printing defects that presents. The porosity percentage is mainly influenced by the water content on the sample and the printing defects related with the size and morphology of the ceramic feedstock. This second defect has not been investigated here, due to it was decided to use the ready to press feedstock (and avoid any post-processing feedstock in order to directly print the AM specimens, and avoid any feedstock treatment, like spray drying, for instance). For this reason, different drying conditions, before sintering, were analysed depending on the water content. During this process, the internal water present on the sample can evaporate itself, but the evaporation rates of the core and the surface are different that is why it is important to compare different drying times.

Figure 4.1 shows the comparison between the three different drying conditions, and its influence on the final density of the samples.

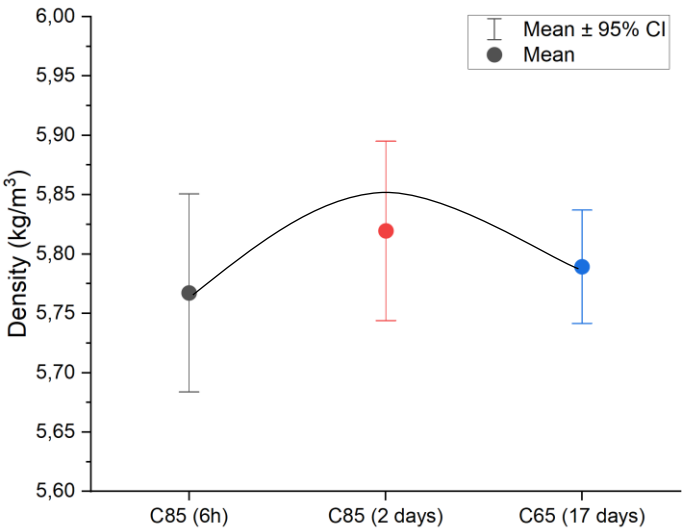

Figure 4.1. *Evolution of the final density of the samples depending on the pre-sintering drying time.*

As it can be seen, the samples from the ***Group A***, have a density of 5.76 ± 0.10 kg/m^3 whereas the samples from ***Group B*** present a density of 5.82 ± 0.08 kg/m^3. On the other hand, samples from ***Group C*** present a density of 5.79 ± 0.02 kg/m^3.

It can be seen a parabolic tendency reaching the maximum density for a drying period of 2 days. This means that the first 2 days have an important impact on the final density of the sample, and once this period is passed, the final density of the samples start to decrease. This phenomenon may be consequence of a drastically evaporation of the water of the sample, creating pores and cracks that the further sintering process of the green body is not able to close and fix.

4.2. Composition and crystalline structure

In ***Figure 4.2***, the XRD spectrum for the polished surface of the cold isostatic press (CIP) 8Y-TZP sample is presented. In this spectrum the main peaks are indexed, while secondary peaks ranged between 45 and 75^o are not. These peaks are related to the cubic phase of zirconia, as reported in Ref. [36], where they used the same powder provided from Tosoh.

As for the printed samples, the XRD pattern is shown in ***Figure 4.3***, it can be seen that they present the same crystallography structure as the CIP one.

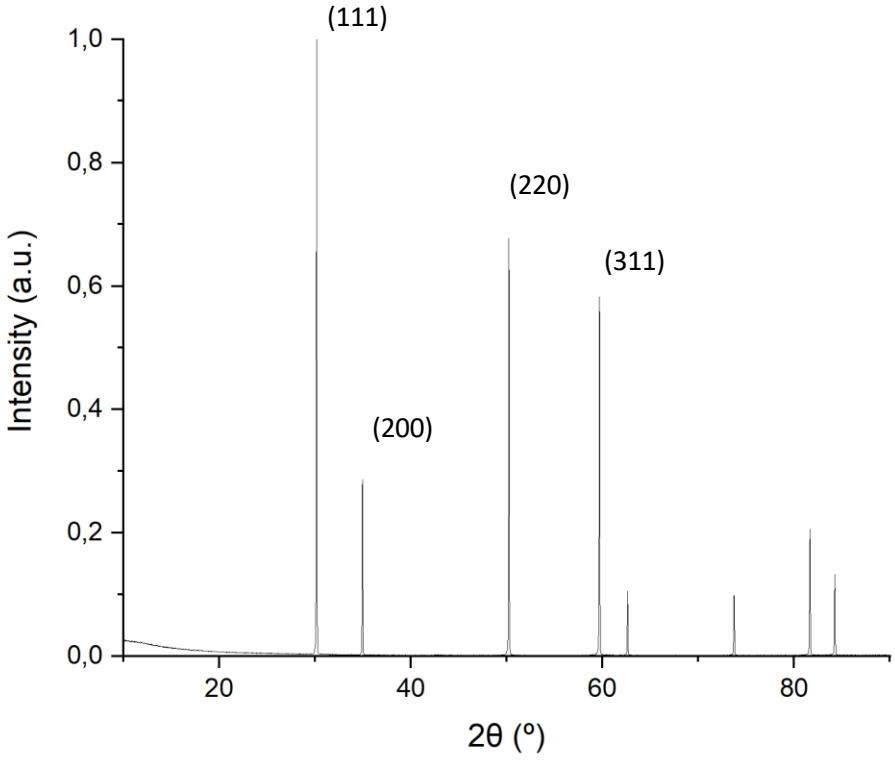

Figure 4.2. *XRD pattern of the 8Y-TZP sample fabricated via CIP.*

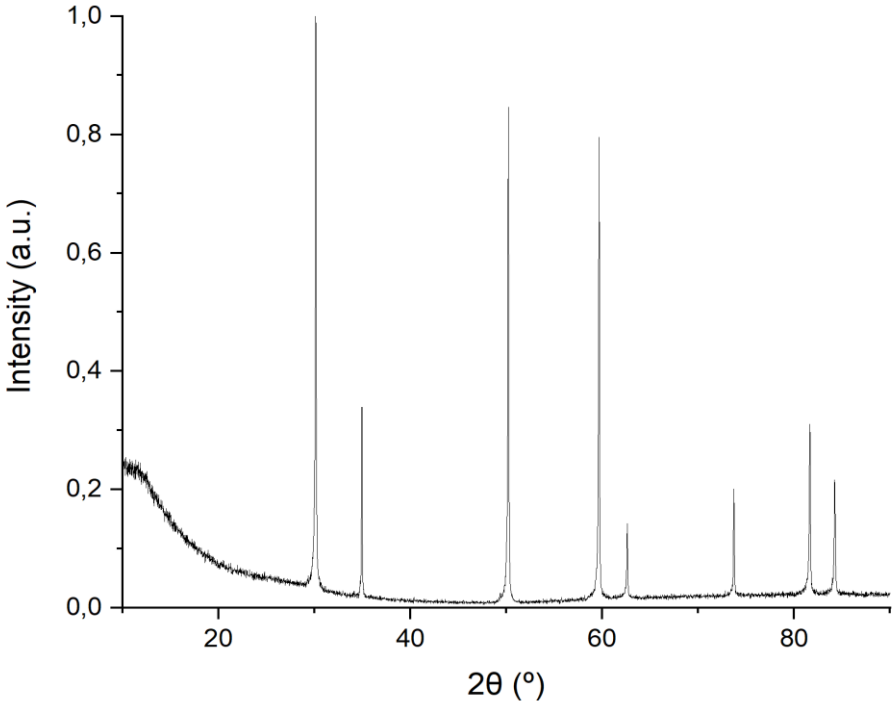

Figure 4.3. *XRD pattern of the 8Y-TZP printed sample.*

4.3. Particle size

In ***Figure 4.4***, it can be seen that the ceramic powder provided by Tosoh present a wide range of particle size distribution, from 0.1 up to 400 μm.

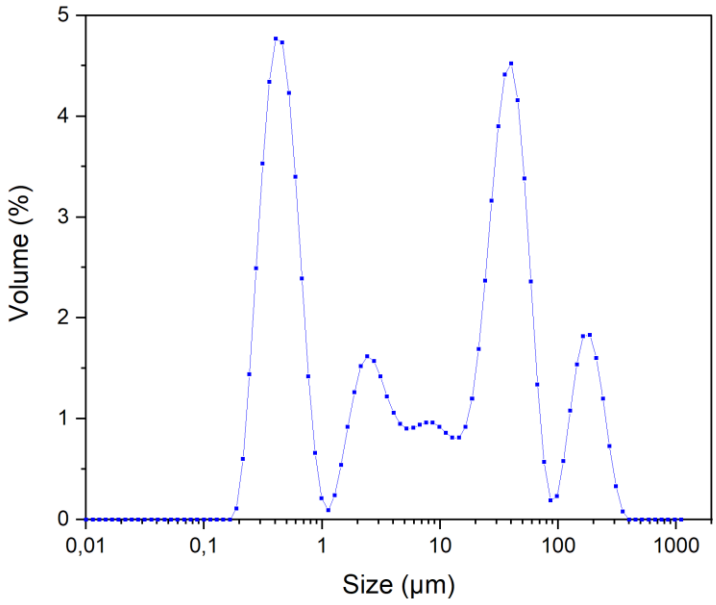

Figure 4.4. *Particle size distribution of the 8Y-TZP provided by Tosoh.*

The feedstock presents 4 different particles size distribution as depicted in ***Figure 4.4*** and summarized in ***Table 4.4***. Where it can be seen that a 10 % of the particles have a size under 0.39 µm, corresponding to the first peak in ***Figure 4.4***, and that the 90 % of the particles have a size under 884.37 µm, which corresponds to the last peak of ***Figure 4.4***.

Table 4.4. *Distribution of the particle's size in the feedstock.*

	Dx (10) (µm)	Dx (50) (µm)	Dx (90) (µm)
Particle size	0.39	24.15	884.37
STDV	0.03	11.81	746.38

In ***Figure 4.5***, a SEM micrograph showing the particle size distribution can be clearly observed. As it is depicted in this micrograph, these data pits perfectly with the particle size distribution presented in ***Figure 4.4***. Within this context, this morphology is not suitable for a 3D printing process, due to the coarse particles can block the nozzle and increase the number of defects in the 3D printed specimen.

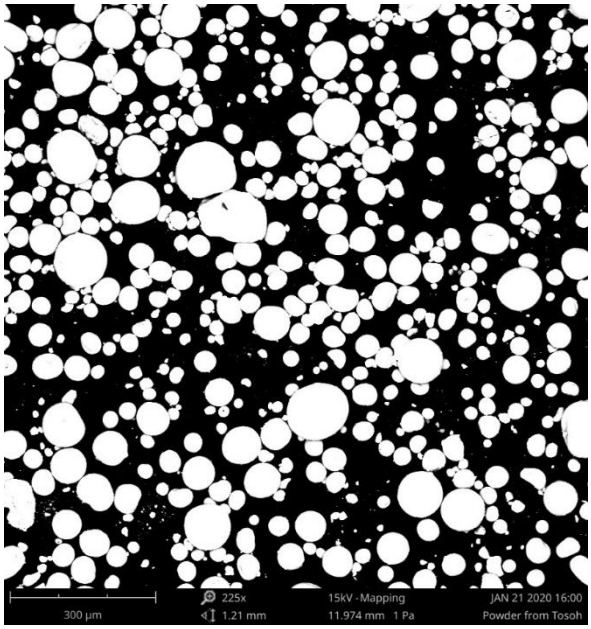

Figure 4.5. *SEM micrograph of the ceramic powder used in this Master's thesis (scale 300 µm).*

The correct determination of the particle size plays an important role for the 3D printing process. It is stablished that the relation of the diameter of the extruded filament is 10 times the mean size of the particle. Thus, the choice of the nozzle used to print will depend on the size of the particle.

In this Master's thesis, it has been used a 0.588 mm diameter nozzle to print the samples. This means that the maximum particle size supported, before obstruction while printing, is approximately 500 µm.

In ***Figure 4.4***, the results found are that the maximum particle size of the powder is 400 μm, which is lower than the limit imposed by the nozzle used during the study. Nevertheless, to achieve a better performance while printing and avoid defects on the final parts, the feedstock should be treated by sieving in order to obtain a mono-modal distribution with a fine particle.

4.4. Rheology: Sol-gel point

The aim of this experiment is to demonstrate that, the 3D printer used during this Master's thesis, is adequate to print the ceramic paste consisting of 25 wt. % of hydrogel and 75 wt. % of ceramic charge (8Y-TZP).

In order to do so, the rheology of the hydrogel (Pluronic F-127 and distilled water) and the ceramic paste (hydrogel and ceramic powder) has been studied. ***Figure 4.6*** shows the gel point of the hydrogel (blue) and the ceramic paste (red). The gel point is where G' = G'', which means that the mixture starts to flow. Thus, it is possible to extract the minimum force, required by the 3D printer, to extrude the mixture through the syringe. Using the ***Eq.4.1*** the minimum force to print can be determined as follows:

$$\tau = \frac{F}{S} \qquad \textbf{(Eq. 4.1)}$$

Where τ is the shear stress (Pa) at G' = G'', F (N) is the minimum force to make the mixture flow and S (m^2) is the section of the syringe.

Substituting the values from ***Figure 4.6*** into **Eq. 4.1**, the minimum force required to print the desired past is found to be around 240 mN.

This printing force F is significantly lower than the maximum force F_{max} = 100 N, that can apply the 3D printer used in this Master's thesis. Hence, the equipment satisfies the rheological necessities of this Master's thesis.

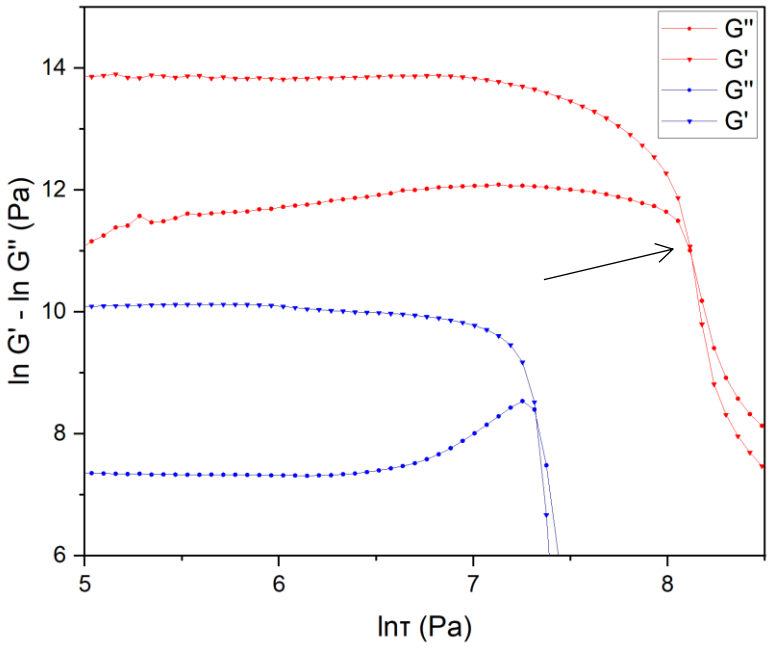

Figure 4.6. *Representation of the rheological behaviour of the hydrogel and the ceramic paste used in this Master's thesis.*

As a final remark, as depicted in ***Figure 4.6*** with an arrow, the introduction of ceramic powder increases significantly the flow stress to make the mixture flow. As it is depicted in ***Figure 4.6***, the flow stress for the gelling agent (Pluronic F-127) is around 18 MPa, while after adding the investigated ceramic charge, this point increases significantly until reaching a final value of 40 MPa. In this sense, the ceramic charge increases by a factor of 1.2 the flow stress point.

4.5. Microstructural and mechanical analysis

4.5.1. CIP sample

An exhausting mechanical and microstructural study of the CIP sample was done. As this is the sample used as a reference all along this Master's thesis, and due to the lack of information of 8Y-TZP both microstructural and mechanical properties it was decided to properly characterise it.

4.5.1.1. Microstructural characterisation

The grain size of the sample was determined using the *Linear Intercept Method* (LIM), using the software ImageJ (more information is available in ***Annex B.2: ImageJ***). To do so, 5 different SEM micrographs (see ***Figure 4.7***) were analysed following the same methodology: 3 vertical and 3 horizontal lines randomly traced through the picture, and a further measurement of each grain interception with these lines. A total of 600 measurements were done in order to get a statistical

signification. In ***Figure 4.8***, it can be seen that the grain size for the sintered specimens and after using the LIM methodology is around 2.4 ± 1.3 µm.

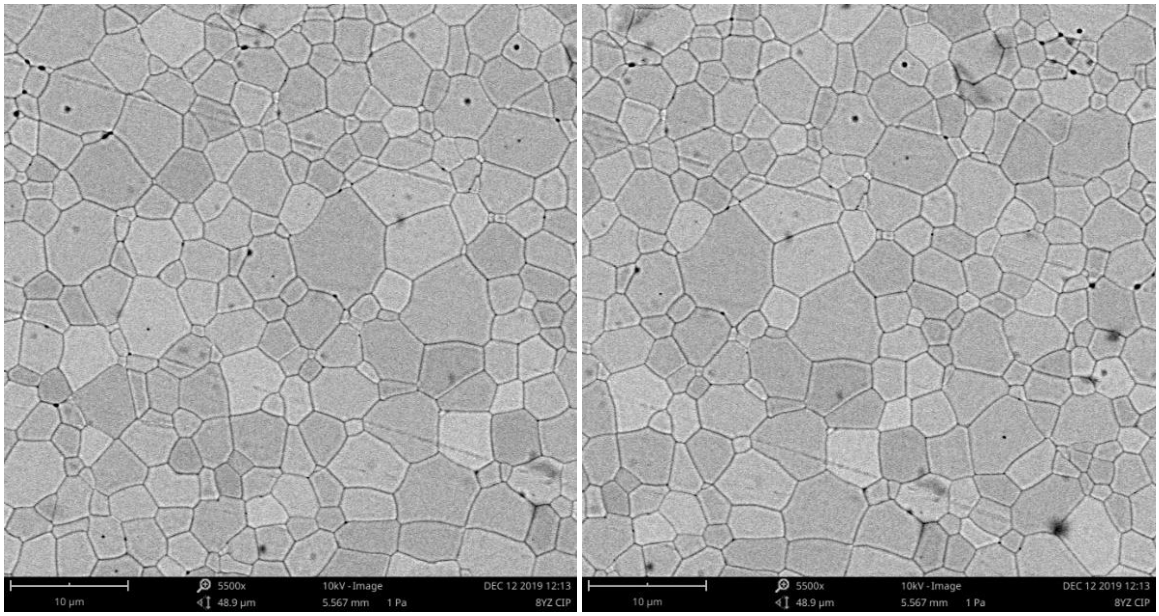

Figure 4.7. *SEM images of the microstructure of the sample at 5500x (scale of 10 µm).*

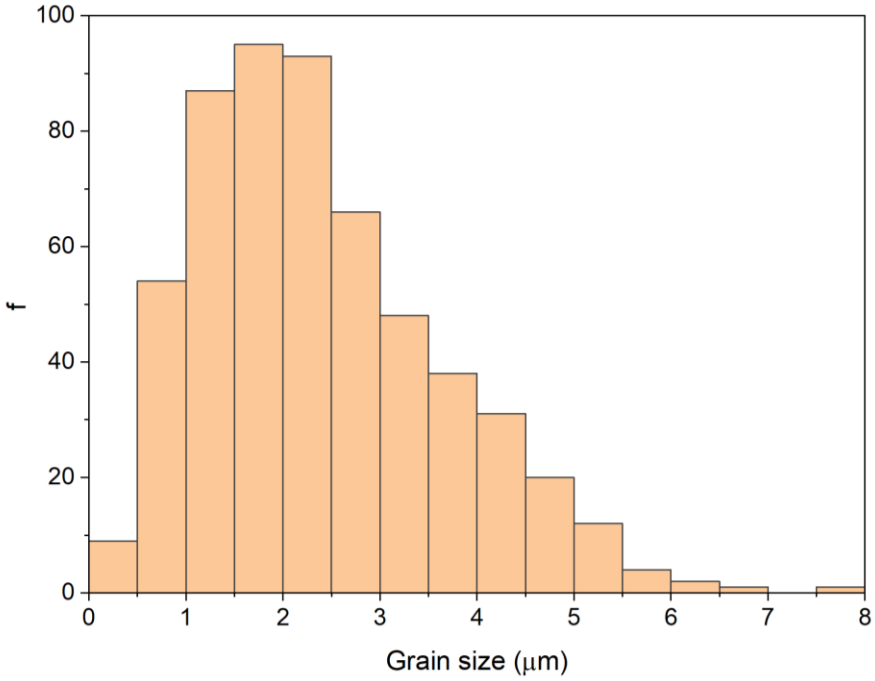

Figure 4.8. *Histogram of the different grain sizes measured in 5 different micrographs for the 8Y-TZP sample.*

4.5.1.2. Mechanical characterisation

A Vickers hardness indentation test was carried out with the CIP sample. Since there is a lack of literature regarding the mechanical properties for the cubic (c)-phase, the purpose of this test was to report the composite hardness values of it. In order to do so, a 10 kgf load was applied to the CIP sample. A total of five indentations were done randomly distributed in order to get a statistical signification. In ***Figure 4.9*** it can be seen a SEM micrograph showing the residual Vickers hardness indentation performed in 8Y-TZP.

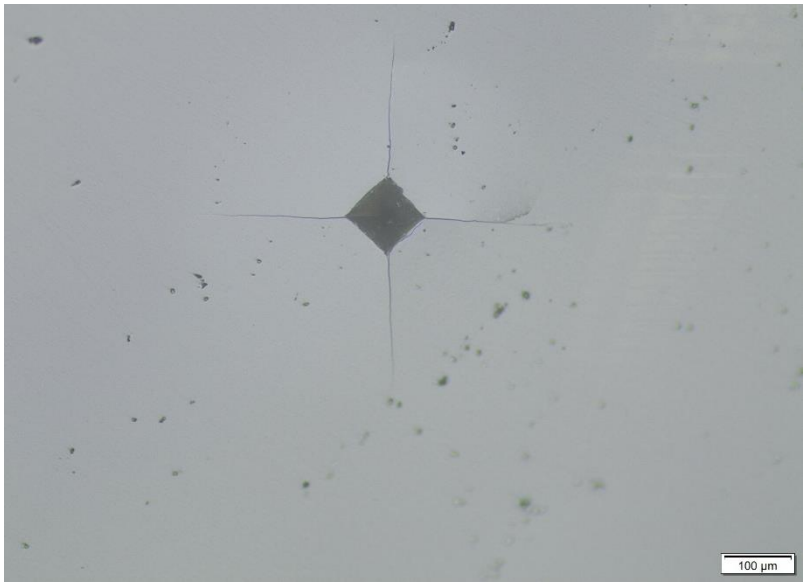

Figure 4.9. *Vickers indentation performed on the CIP sample.*

The diagonals length was measured using the *ImageJ* software (***Annex B.2***: ImageJ). The final Vickers hardness (HV) values of the CIP sample is 13.7 ± 0.4 GPa.

The same methodology was used to determine the HV value of the 3D printed parts. However, the indentations were realised in the transversal section of the part, in order to examine the mechanical properties of the filament's cohesion. A total of 5 indentations of 1 kgf load (see ***Figure 4.10***) were applied to the sample. The HV for the investigated specimen is around 15.0 ± 0.6 GPa. Furthermore, as it clearly evident in this image, the residual cracks induced at the edges of the residual imprint are not evident for the 3D printed specimen due to the superficial defectology do not lead a correct observation and measurement of the crack length and as a consequence the correct determination of the indentation fracture toughness as we will explain in more detail in ***section 4.7***.

This values are in fair agreement with those reported in Ref. [37], where they used the same ceramic powder from Tosoh. Even though they used a different 3D printing technique, they report very similar hardness values to the ones found in this Master's thesis. The values for their printed parts range from 14.5 to 15.3 GPa. In addition, for the CIP sample they report hardness values of 11 to 13.7 GPa.

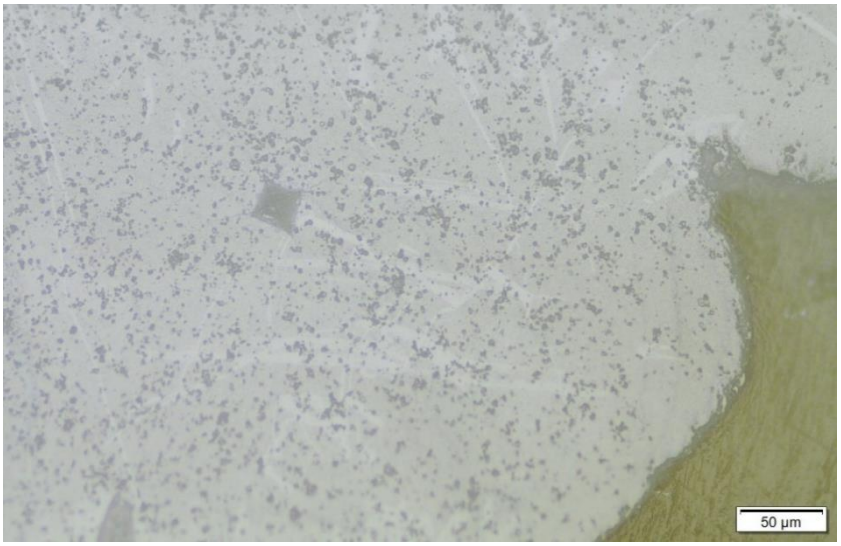

Figure 4.10. *Vickers indentation performed on a 3D printed sample.*

4.6. Mechanical properties: Nano-hardness and elastic modulus

From the Berkovich indentations (see ***Figure 4.11***) values performed at 2000 nm of maximum displacement into surface (or until reach 650 mN of maximum applied load), it is possible to observe the hardness (*H*) and the elastic modulus (*E*) evolution against the displacement into surface for the different specimens performed along this Master's thesis in order to try to correlate the micromechanical properties with the different drying conditions (see ***Table 4.1, Table 4.2, Table 4.3***) as well as to compare them to the sample manufactured by conventional processing.

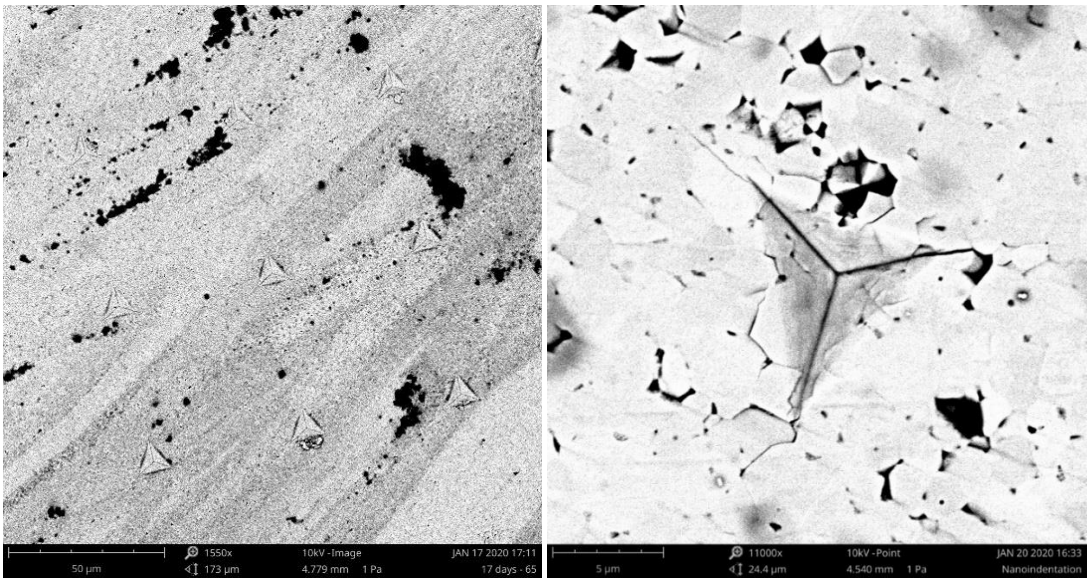

Figure 4.11. *From left to right: Overall sight of nanoindentation prints on a 3D printed sample (scale of 50 µm), and micrography of an imprint on a 3D printed sample (5 µm).*

In ***Figure 4.13***, it is depicted the average hardness, obtained by nanoindentation for the different specimens as a function of the different drying times investigated here. All these data, are compared to the reference sample. The results show that the hardness of the samples does not change drastically with the drying time. In addition, it is shown that only exists a maximum difference of an 8.1 % between the hardness of the 3D printed samples and the CIP sample. This difference may be associated with the pre-existing porosity already observed for the 3D printed specimens, see ***Figure 4.10***.

On the other hand, the elastic modulus mainly depends on the chemical composition and the porosity (in this Master's thesis mainly attributed to printing defects) of the affected zone . As demonstrated by using the XRD technique (in ***section 4.2***), the chemical composition of both samples, 3D printed and CIP, is the same due to the main peaks of the XRD diffractogram fits perfectly. In this sense, the only parameter that can affect the elastic modulus is the porosity randomly distributed in the 3D printed sample. However, the problem of the nanoindentation technique is that is a local experiment and its effect in terms of the elastic (*E*) and plastic (P) deformation zone can be seen in ***Figure 4.12***, where P is 7 to 10 times h_{max} (14-20 µm) and E is 20 times h_{max} (40 µm). It may be possible that a defect such as porosity, would be in this P and E deformation zones giving non-representative values.

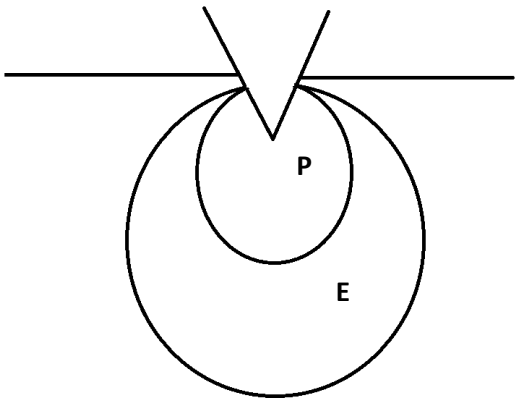

Figure 4.12. *Schematic representation of the elastic and plastic deformation zone produced during a nanoindentation.*

In ***Figure 4.14*****,** it is depicted the average elastic modulus of all different investigated specimens. Here, samples from group B and C present higher elastic modulus than the CIP sample, with a maximum difference of 20.7 %. This fact could be due to what it has been explained before. Furthermore, according to Ref. [32], nanoindentation technique is sensitive to the presence of submicrometric defects in materials, such as residual porosity or microcracks generated during the sintering process. In addition, this technique is also sensitive to the sample's roughness, which in this Master's thesis is affected by the polishing process because the *c*-ZrO_2 grains are detached from the sample during this process. All these limitations could be an explanation of the elastic modulus' values found in this Master's thesis.

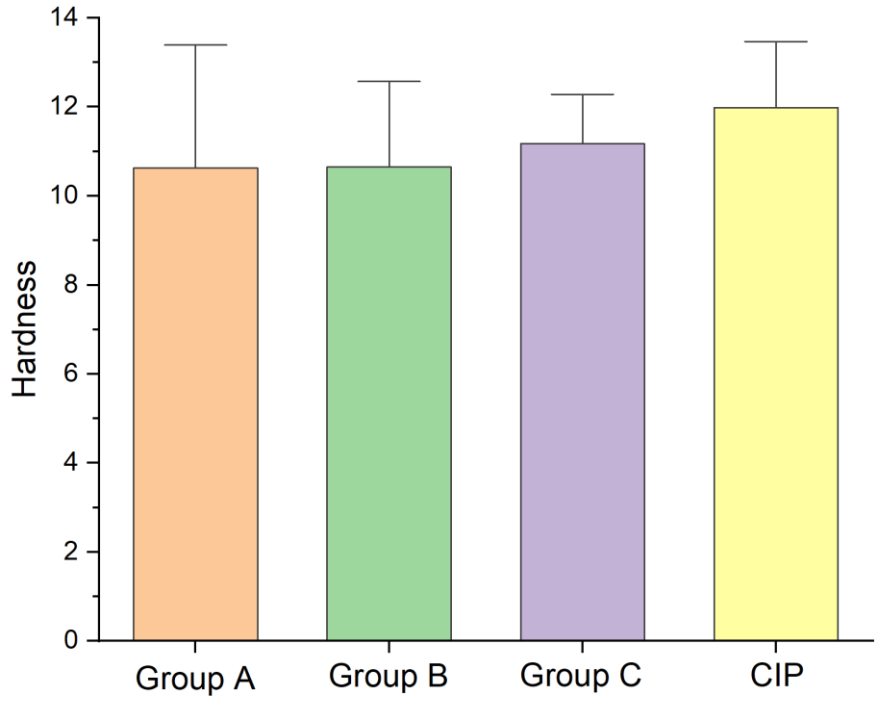

Figure 4.13. *Average hardness of the samples tested during this Master's thesis.*

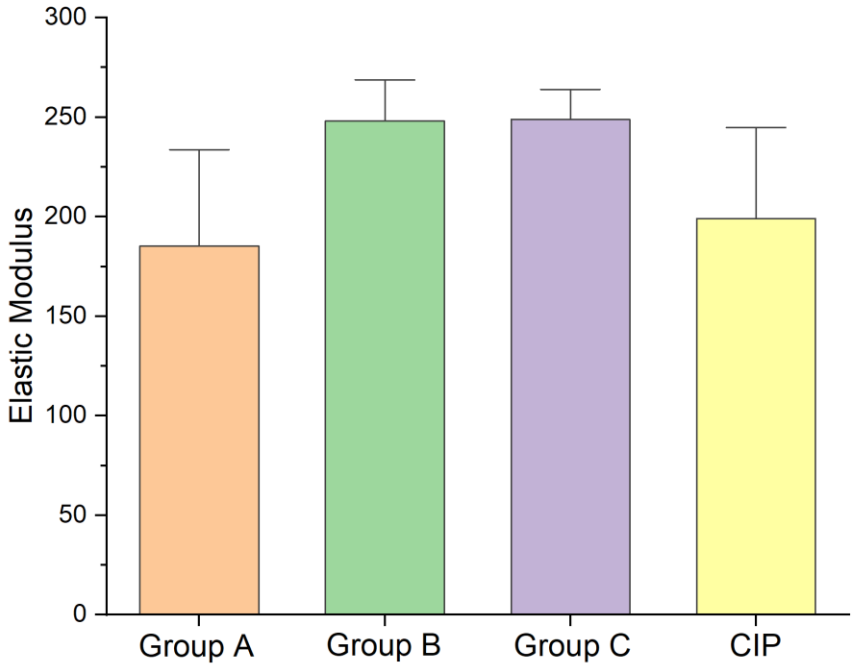

Figure 4.14. *Average elastic modulus of the samples tested during this Master's thesis.*

To sum up, as it is evident in these images, the specimen present pre-exiting porosity mainly induced during the previous stage prior the sintering process. More information related to this defectology can be found in ***section 4.7***.

4.6.1. Fracture toughness

In addition, the fracture toughness of the CIP sample was determined by the *Niihara* method [38] using the values of Vickers hardness (see ***section 4.5.1.2***) and the values of elastic modulus encountered with the nanoindentation study (see ***section 4.6***). Due to the imprecisely values of elastic modulus determined for the printed parts, the determination of the fracture toughness was dismissed.

The approximative value of fracture toughness encountered, for the CIP specimen using E = 199 GPa, is 3.0 ± 0.1 MPa·$m^{1/2}$. This value is in the range of 1.79 ± 0.11 and 3.16 ± 0.06 MPa·$m^{1/2}$ proposed by [37] and [39].

4.7. Defectology

The main defect encountered along this Master's thesis was consequence of the water evaporation of the samples. As it can be seen in ***Figure 4.15***, the sintered samples presented cracks due to the water evaporation rates during the sintering process. The evaporation rate of the core of the sample is slower than the superficial evaporation rate causing cracks in the external part of the samples.

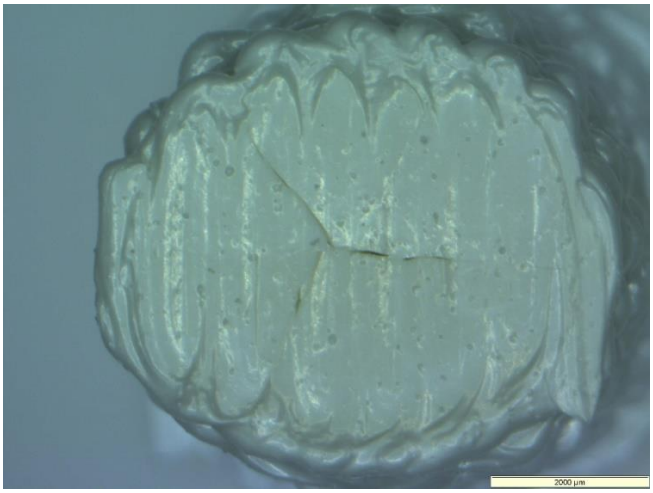

Figure 4.15. *Sintering defects of a cylindrical sample (scale of 2000 µm).*

As explained in ***section 4.1***, the tubular samples were finally dismissed of the study because they all broke as consequence of crack formation during the sintering process. In ***Figure 4.16***, it can be seen an internal crack going from the core to the surface of the sample, also due to an abrupt water evaporation during the sintering process.

Figure 4.16. *SEM image of a tubular 3D printed sample (scale of 100 µm).*

In order to reduce this problem, it is possible to print the parts with an interior support material as hydrogel or oil, to maintain an hydrostatic pressure inside the part and reduce the crack formation due to the rapidly water evaporation of the surface.

4.8. Micro-compression

One of the tests that was intended to be carried during this Master's thesis was the micro-compression of the tubular samples. This experiment would have been of great interest in order to know the maximum height, before a decohesion of the layers, for a 3D printed electrolyte as well as in order to investigate the adhesion between layers. However, as explained before, the tubular samples broke after the sintering process and the test was consequently dismissed. Nevertheless, a preliminary test was carried out with a cubic sample of dimensions of 5.5 x 5.5 mm, in order to find the right parameters to test this kind of samples.

In ***Figure 4.17***, it is shown the results of the micro-compression test. It can be seen three apparent regimes characteristic of materials with internal porosity, as explained in [40]. The first regime is

The first regime of the curve is due to the accommodation effect between the sample and the platter's press. Afterwards, a linear tendency due to the elastic behaviour of the part can be observed, until the part fails because of an internal defect. However, it can be observed a densification process (serrated zone) due to the presence of internal porosity heterogeneously distributed along the entire specimen on the second region of the curve, where the microporosity is being closed by the compressive load applied. This phenomenon can be seen on the third region of the curve until the part completely fails.

This is just a preliminary test that will open further investigations in CIEFMA's group in order to find more accurate results.

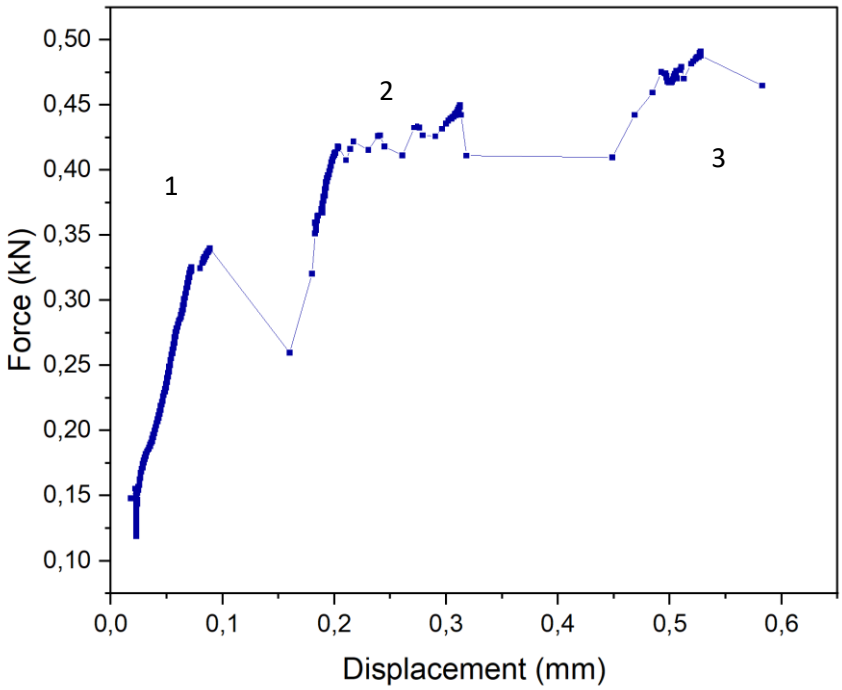

Figure 4.17. *Force vs. displacement of the micro-compression test performed with a cubical geometry 8Y-TZP sample.*

5. Environmental impact analysis

In general terms, in this Master's project, the environmental impact is related to the materials used to prepare the samples and during the processing process as well as the energy consumption associated to the thermal treatments, polishing process and the machines employed to microstructurally and mechanically characterize the material.

The materials used throughout the project do not have a high harm for the environment. During the ceramic paste preparation, all waste and leftover was tried to avoid by always preparing small amounts of ceramic paste.

As far as the processing process, the printing material; syringe, piston and nozzle, were reused as far as possible, instead of using it as disposable materials. The main environmental problem was the use of the furnace that has a huge energy consumption. Another problem was the polishing process. Though it, a lot of water was used and the grind paper to polish was a disposable one. Hence, there was some waste products generation, but they were rightly recycled.

Finally, through the characterization process, electrical energy was consumed but in comparison to the electrical consumption associated to the furnace, it is insignificant.

6. Conclusions

The results of this Master's thesis draw the following conclusions:

In order to get the best **microstructural** and **mechanical** properties, the following printed and sintered conditions may be taken into consideration:

- The composition of the ceramic paste should be 70 wt. % of ceramic 8Y-TZP charge and 25 wt. % of hydrogel composed by Pluronic F-127 and distilled water. These chemical composition leads to provide a 3D printed specimen with a 97-98 % of the theoretical density.
- Store the printed specimen a minimum of 2 days in a relative humid atmosphere (around 85 %) before the sintering process leads to obtain the maximum relative density of the final part.
- For the printing process the most important parameter is the printing speed in order to let dry and gain consistency the already printed layers.

The printed specimens present up to 98 % relative density compared to the specimen fabricated by a conventional processing technique, in particular with the specimens performed by using the cold isostatic pressing methodology.

It has been demonstrated that the 3D printing specimens present similar *micro*- and *nano*- mechanical properties with the sample fabricated by a conventional processing route.

In terms of the Vickers Hardness, the 3D printed specimens presented higher values than the specimen produced by CIP. As far as for the nanoindentation hardness and elastic modulus, the 3DP parts presented similar values of hardness. Nevertheless, it has been found that the values found for the elastic modulus are sensitive to different aspects such as the porosity and the roughness of the parts, giving less concise values.

Concerning the reduction of printing defects, it is recommended to treat the feedstock before printing in order to achieve an homogenous particle size of the powder and be able to use a nozzle with a smaller diameter in order to enhance the resolution of the final 3D printed part.

Finally, it would be interesting to follow the investigation of microcompression of the printed samples in order to extract the compression elastic modulus value through a different experiment and compare it to the nanoindentation technique. Furthermore, in the compression stress-strain curve obtained for the 3D printed specimen it is clearly evident to observe a densification process (serrated zone) due to the presence of internal porosity heterogeneously distributed along the entire specimen.

To sum up, the final conclusion of this Master's thesis is that it is possible to print *c*-ZrO_2 by additive manufacturing method with the same density and mechanical properties than with conventional technique such as cold isostatic pressing.

7. Budget and financial analysis

***Table 7.1**. Summary of the cost of consumables used in this Master's thesis.*

CONSUMABLES			
Product	**Quantity**	**Cost/ud.**	**Cost**
Pluronic F-127	0.4 Kg	190 €/Kg	76 €
8Y-TZP	0.3 Kg	125 €/Kg	37.50 €
Distilled water	1Kg	0.7 €/Kg	0.70 €
Grinding paper P120	5	0.8 €/un.	4 €
Grinding paper P320	5	0.8 €/un.	4 €
Grinding paper P600	5	0.8 €/un.	4 €
Grinding paper P1200	5	0.8 €/un.	4 €
Cloth MD-Dac	2	53 €/un.	106 €
Cloth MD-Nap	1	75 €/un.	75 €
Diamond suspension 6µm	0.1 L	83 €/L	8.30 €
Diamond suspension 3µm	0.1 L	75 €/L	7.50 €
Colloidal silica suspension	0.1 L	150 €/L	15 €
Acetone	0.2 L	8 €/L	1.60 €
Epoxy resin	0.1 L	11.16 €/L	1.12 €
Parafilm	0.25	50 €/un.	12.5 €
Subtotal			**357.22 €**

Table 7.2. *Summary of the equipment used in this Master's thesis.*

EQUIPMENT			
Equip	**Quantity**	**Cost/ud.**	**Cost**
Balance	5 h	10.3 €/h	51.50 €
SpeedMixer	5 h	5 €/h	25 €
3D Printer	40 h	12.4 €/h	500 €
Nabathern Furnace	140 h	12.4 €/h	1736 €
Polisher LaboPol-5	20 h	12.4 €/h	248 €
OM	2 h	13.45 €/h	26.90 €
Nanoidenter	20 h	60 €/h	1200 €
SEM	10 h	150 €/h	450 €
XRD	2 measures	22.44 €	44.88 €
Magnify lent	5 h	7 €/h	35 €
Vickers indenter	2 h	12.4 €/h	24.8 €
Subtotal			**4342.1 €**

Table 7.3. *Summary of the personal costs employed in this Master's thesis.*

COST OF SUPPORT ENGINEERING			
Concept	Quantity	Cost/ud.	Cost
Support technician	20	40 €/h	800 €
Supervisor	25 h	50 €/h	1250 €
Subtotal			**2050 €**

Table 7.4. *Summary of the cost of the engineering designer.*

COST OF ENGINEERING BY THE DESIGNER			
Sample preparation	200 h	24.8 €/h	4960 €
Sample Characterization	80 h	24.8 €/h	1984 €
Search for information	100 h	24.8 €/h	2480 €
Analysis results	80 h	24.8 €/h	1984 €
Memory development	380 h	24.8 €/h	9424 €
SUBTOTAL:			**20832 €**

Table 7.5. *Summary of the total cost of the project.*

TOTAL COST OF THE PROJECT	
Concept	**Cost**
Total cost associated with consumables	**357.22 €**
Total cost associated with the sample characterisation	**4342.1 €**
Total cost associated with the engineering	**20832 €**
Total cost associated with suport engineering	**2050 €**
TOTAL	**27581.32 €**
IVA (21 %)	**5792.10 €**
TOTAL + IVA	**33373.40 €**

References

[1] S. Edition and W. Virginia, "Fuel cell handbook," *Choice Rev. Online*, vol. 26, no. 11, pp. 26-6292-26–6292, 1989.

[2] L. Carrette, K. A. Friedrich, and U. Stimming, "Fuel Cells: Principles, Types, Fuels, and Applications," *CHEMPHYSCHEM*, vol. 1, pp. 162–193, 2000.

[3] H. Vaghari, H. Jafarizadeh, A. Berenjian, and N. Anarjan, "Recent Advances in Application of Chitosan in Fuel Cells," *Sustain. Chem. Process.*, vol. 1, p. 16, Sep. 2013.

[4] N. Q. Minh and T. Takahashi, "Chapter 2 - Principles of operation," in *Science and Technology of Ceramic Fuel Cells*, 1995, pp. 15–40.

[5] N. Q. Minh and T. Takahashi, "Introduction," in *Science and Technology of Ceramic Fuel Cells*, no. iii, Elsevier B.V, 1995, pp. 1–14.

[6] "Toyota Motors." [Online]. Available: https://www.toyota-europe.com/world-of-toyota/feel/environment/better-air/fuel-cell-vehicle#/gallery/11-555068/2. [Accessed: 16-Oct-2019].

[7] J. W. Pratt, "Maritime Fuel Cell Generator Project Project ID # MT013," no. May, 2015.

[8] N. Q. Minh and T. Takahashi, "Chapter 5 - Cathode," in *Science and Technology of Ceramic Fuel Cells*, 1995, pp. 117–146.

[9] N. Q. Minh and T. Takahashi, "Chapter 6 - Anode," in *Science and Technology of Ceramic Fuel Cells*, 1995, pp. 147–164.

[10] N. Q. Minh and T. Takahashi, "Chapter 4 - Electrolyte," in *Science and Technology of Ceramic Fuel Cells*, no. iii, 1995, pp. 69–107.

[11] M. C. F. and F. B. Cláudia Ângela Maziero Volpato, Luis Gustavo D´Altoé Garbelotto, "Application of Zirconia in Dentistry: Biological, Mechanical and Optical Considerations," *Intech Open*, p. 13, 2011.

[12] Y. Han and J. Zhu, "Surface science studies on the zirconia-based model catalysts," *Top. Catal.*, vol. 56, no. 15–17, pp. 1525–1541, 2013.

[13] M. M. Abdul-Monem, "Overview of zirconia," 2017. [Online]. Available: https://www.slideshare.net/MohamedMahmoud443/zirconia-overview. [Accessed: 17-Nov-2019].

[14] C. Piconi and G. Maccauro, "Oxide Ceramics for Biomedical Applications," *Ref. Modul. Mater. Sci. Mater. Eng.*, no. March 2015, 2016.

[15] A. Paterson, "Phase analysis of sintered yttria-zirconia ceramics by x-ray diffraction," pp. 295–299, 1986.

[16] T. Moritz and S. Maleksaeedi, *Ceramic Components*. Elsevier Inc., 2018.

[17] K. S. Prakash, T. Nancharaih, and V. V. S. Rao, "Additive Manufacturing Techniques in Manufacturing -An Overview," *Mater. Today Proc.*, vol. 5, no. 2, pp. 3873–3882, 2018.

[18] H. Geng, H. Song, J. Qi, and D. Cui, "Sustained release of VEGF from PLGA-nanoparticles mbedded thermo-sensitive hydrogel in full-thickness porcine bladder acellular matrix," *Nanoscale Res. Lett.*, vol. 6, no. 1, p. 312, 2011.

[19] J. C. Gilbert, J. L. Richardson, M. C. Davies, K. J. Palin, and J. Hadgraft, "The effect of solutes and polymers on the gelation properties of pluronic F-127 solutions for controlled drug delivery," *J. Control. Release*, vol. 5, no. 2, pp. 113–118, 1987.

[20] M. S. Hamid Akash, K. Rehman, and S. Chen, "Natural and synthetic polymers as drug carriers for delivery of therapeutic proteins," *Polym. Rev.*, vol. 55, no. 3, pp. 371–406, 2015.

[21] Q. Dou, A. A. Karim, and X. J. Loh, "Modification of thermal and mechanical properties of PEG-PPG-PEG copolymer (F127) with MA-POSS," *Polymers (Basel).*, vol. 8, no. 9, pp. 1–14, 2016.

[22] F. Bachelor and P. Materials, "Materials engineering degree 3D PRINTING OF SOLID OXIDE FUEL CELLS Report and Annexes," no. June, 2018.

[23] F. M. Project, "Final Master Project : Materials engineering degree 3D-PRINTING OF 8Y-TZP SOLID OXIDE FUEL CELL ELECTROLYTES Report and Annexes," no. February, 2019.

[24] "Mastersizer 3000 | World's Leading Particle Size Analyzer." [Online]. Available: https://www.malvernpanalytical.com/en/products/product-range/mastersizer-range/mastersizer-3000. [Accessed: 19-Jan-2020].

[25] D. Weitz, H. Wyss, and R. Larsen, "Oscillatory rheology: Measuring the viscoelastic behaviour of soft materials," *GIT Lab. J. Eur.*, vol. 11, no. 3–4, pp. 68–70, 2007.

[26] H. H. Winter and F. Chambon, "Analysis of Linear Viscoelasticity of a Crosslinking Polymer at the Gel Point," *J. Rheol. (N. Y. N. Y).*, vol. 30, no. 2, pp. 367–382, Apr. 1986.

[27] Y. Fernández, "2015 Guía del usuario P1503023-UPC-BCN3D+ Dual Paste," 2015.

[28] B.S.Majumdar, "FE-SEM Principle," *New Mex. Tech-Materials Dep. New Mex.*, 2009.

[29] I. Standard, "ISO 6507 - Vickers Hardness Test," vol. 1997, 1997.

[30] "SURFACE Nanolab …always one step ahead." [Online]. Available: http://www.surface-tec.com/nanotips.php. [Accessed: 12-Jan-2020].

[31] W. C. Oliver and G. M. Pharr, "Measurement of hardness and elastic modulus by instrumented indentation: Advances in understanding and refinements to methodology," *J. Mater. Res.*, vol. 19, no. 1, pp. 3–20, Jan. 2004.

[32] J. Roa *et al.*, "Mechanical Characterisation at Nanometric Scale of a New Design of SOFCs," *Fuel Cells*, vol. 11, pp. 124–130, Feb. 2011.

[33] J. J. Roa, X. G. Capdevila, M. Martínez, F. Espiell, and M. Segarra, "Nanohardness and Young's modulus of YBCO samples textured by the Bridgman technique," *Nanotechnology*, vol. 18, no. 38, p. 385701, Sep. 2007.

[34] N. Khlystov and J. Zheng, "Uniaxial Tension and Compression Testing of Materials," pp. 1–19, 2013.

[35] I. D. Marinescu and M. Pruteanu, *Deformation and Fracture of Ceramic Materials*, Second Edi. Elsevier Inc., 2015.

[36] L. Ferrage, G. Bertrand, and P. Lenormand, "Dense yttria-stabilized zirconia obtained by direct selective laser sintering," *Addit. Manuf.*, vol. 21, no. January, pp. 472–478, 2018.

[37] A. Ghazanfari, W. Li, M. C. Leu, J. L. Watts, and G. E. Hilmas, "Additive manufacturing and mechanical characterization of high density fully stabilized zirconia," *Ceram. Int.*, vol. 43, no. 8, pp. 6082–6088, 2017.

[38] G. Quinn, "Fracture Toughness of Ceramics by the Vickers Indentation Crack Length Method: A Critical Review," *A Crit. Rev.*, vol. 27, pp. 45–62, Mar. 2006.

[39] M. Morales, J. J. Roa, X. G. Capdevila, M. Segarra, and S. Piñol, "Mechanical properties at the nanometer scale of GDC and YSZ used as electrolytes for solid oxide fuel cells," *Acta Mater.*, vol. 58, no. 7, pp. 2504–2509, 2010.

[40] V. Canseco, Y. Anguy, J. J. Roa, and E. Palomo, "Structural and mechanical characterization of graphite foam/phase change material composites," *Carbon N. Y.*, vol. 74, pp. 266–281, 2014.

Annex

Annex A: Data sheets

Annex A.1: Pluronic F-127 Sigma Aldrich

SIGMA-ALDRICH®

sigma-aldrich.com

3050 Spruce Street, Saint Louis, MO 63103, USA
Website: www.sigmaaldrich.com
Email USA: techserv@sial.com
Outside USA: eurtechserv@sial.com

Product Specification

Product Name:
Pluronic® F-127 - powder, BioReagent, suitable for cell culture

Product Number: **P2443**
CAS Number: 9003-11-6
MDL: MFCD00082049

TEST	Specification
Appearance (Color)	White
Appearance (Form)	Powder
Solubility (Color)	Colorless
Solubility (Turbidity) 50 mg/mL, H2O, at less than 10 deg C	Clear
pH (2.5% solution)	6.0 - 7.0
Moisture Content	≤ 0.75 %
Cell Culture Test	Pass
Recommended Retest Period 2 Years	----------
Note Pluronic is a registered trademark of BASF SE.	----------

Specification: PRD.1.ZQ5.10000051983

Annex A.2: Zirconia powder from Tosoh

Powder Characteristics and Properties

	TZ-3Y-E (TZ-3YB-E)	TZ-3YS-E (TZ-3YSB-E) (TZ-3YSB-C)	TZ-4Y	TZ-6Y	TZ-8Y	TZ-8YS (TZ-8YSB)	TZ-10YS	TZ-3Y20A (TZ-3Y20AB)	TZ-0
Y_2O_3 (mol%)	3	3	4	6	8	8	10	3	0
Actual Particle Size (μm)	0.04 (40nm)	0.09 (90nm)	0.04 (40nm)			0.09 (90nm)		–	0.04 (40nm)

Powder Characteristics

Y_2O_3 (wt%)	5.2 ± 0.5	7.0 ± 0.6	10.3 ± 0.6	13.3 ± 0.6	15.9 ± 0.7	3.9 ± 0.3	–
Al_2O_3 (wt%)	0.1 ~ 0.4	≦ 0.1				18 ~ 22	≦ 0.1
SiO_2 (wt%)	≦ 0.02						
Fe_2O_3 (wt%)	≦ 0.01						
Na_2O (wt%)	≦ 0.04	≦ 0.06	≦ 0.12			≦ 0.04	≦ 0.04
Specific Surface Area (m^2/g)	16 ± 3	7 ± 2	16 ± 3		7 ± 2	6 ± 2	15 ± 3	14 ± 3

Typical Properties of Sintered Body

Density (g/cm^3)	6.05	6.05	6.02	5.90	5.80	5.50	–
Bending Strength R.T. (MPa)*1	1200	1000	500	300	200	2000 (HIPing)	–
Hardness(Hv10)*2	1250					1400	–

*1 : JIS R1601(3-point bending test) *2 : JIS R1610 (Loads : 98.07N)

Annex A.3: *Nordson EFD Optimum® Systems* nozzle

SMOOTHFLOW TAPERED TIPS

Gauge	Color	ID mm	ID Inch	Standard	Opaque Rigid	QTY
14	Olive	1.60	0.063	7018052	7018049	50
16	Grey	1.19	0.047	7018100	7018097	50
18	Green	0.84	0.033	7018158	7018147	50
20	Pink	0.58	0.023	7005009	7005006	50
22	Blue	0.41	0.016	7018298	7005007	50
25	Red	0.25	0.010	7018391	7018370	50
27	Clear	0.20	0.008	7018417	n/a	50

Use with gel cyanoacrylates, UV-cure adhesives, sealants, and particle-filled materials or any medium to high viscosity fluid. Standard tips are molded of polyethylene with UV-light block additive. Rigid, opaque tapered tips are molded of polypropylene and the opacity delivers light-blocking functionality.

CHAMFERED TIPS

Gauge	Color	ID mm	ID Inch	38.1 mm (1.50")	12.7 mm (0.50")	6.35 mm (0.25")	QTY
18	Green	0.84	0.033	n/a	7018129	n/a	50
20	Pink	0.61	0.024	7018188	n/a	n/a	50
22	Blue	0.41	0.016	7018281	n/a	n/a	50
23	Orange	0.33	0.013	n/a	7018321	n/a	50
25	Red	0.25	0.010	n/a	7018352	n/a	50
27	Clear	0.20	0.008	n/a	n/a	7015236	50
33	Clear	0.10	0.004	n/a	n/a	7018482	25
33	Black	0.10	0.004	n/a	n/a	7018477	25

Use for microdot application of low viscosity fluids.

Annex B: Software

Annex B.1: Slic3r

Available: http://slic3r.org/, visited 15/12/2019

Slic3r is the tool you need to convert a 3D model into printing instructions for your 3D printer. It cuts the model into horizontal slices (layers), generates toolpaths to fill them and calculates the amount of material to be extruded.

This free program is used in the university to generate the Gcode. Files directly used in the 3D-printing machine. It gives the possibility of modifying the main printing parameters: infill of the layer, the geometry of the infill and the printing velocity. Also, this program needs some inputs parameters for print like the size of the nozzle and the size of the printing bed.

In the following part, a brief explanation of the inputs used during this Master's thesis will be presented:

1. First of all is important to export the *STL.* file and go to *File* → *Export Conf Bundle* → and select the file of the extruder that you are going to use.
2. The first parameter that you need to modify is the *Printing Settings* (***Figure B.0.1.*** Main display of Slic3r.). In ***Figure B.0.2.a*** are presented all the parameters.
    - **a. Layers and perimeters:**
        - i. *Layer height: h* = Diameter of the nozzle - (0.1*diameter of the nozzle) in both options.
        - ii. *Vertical shells* (for perimeters): *perimeter* = 1 and choose *Spiral vase*.
        - iii. *Quality* (for perimeters): choose all four options.
    - **b. Infill:**
        - i. *Infill*: The *Fill density* for this Master's thesis is 100% for tubular geometry and 100% for the cylindrical geometry. The *Fill pattern* and *Top/bottom fill pattern* → *Rectilinear*.
        - ii. *Advanced*: In this option is just needed to modify the *Fill angle* for both geometries, every layer will be rotating 90º, to get better mechanical properties.
    - **c. Speed:**
        - i. *Speed for print moves:* see ***Table 3.1*** for all speed values used in this Master's thesis. However, keep in mind that for *External perimeters*, *Support material* and *Support material interface*, is important to keep the default values.
        - ii. *Speed for non-print moves*: Reduce the velocity to 20 mm/s.

d. Skirt and brim:

i. *Skirt*: *Loops* = 1.

3. The following parameter is the *Printer Settings* (***Figure B.0.2***). In the ***Figure B.0.2.b*** all the parameters are depicted.

a. General:

i. Size and coordinates:

- *Bed size*: *x* = 110; *y* = 240 mm.
- *Print center*: *x* = 55; *y* = 120 mm.
- *Z offset*: In this option you can modify the starting printing height. Usually, is set to zero.

b. - Extruder 1:

i. *Size*: *Nozzle diameter* →the diameter of the nozzle that you are going to use.

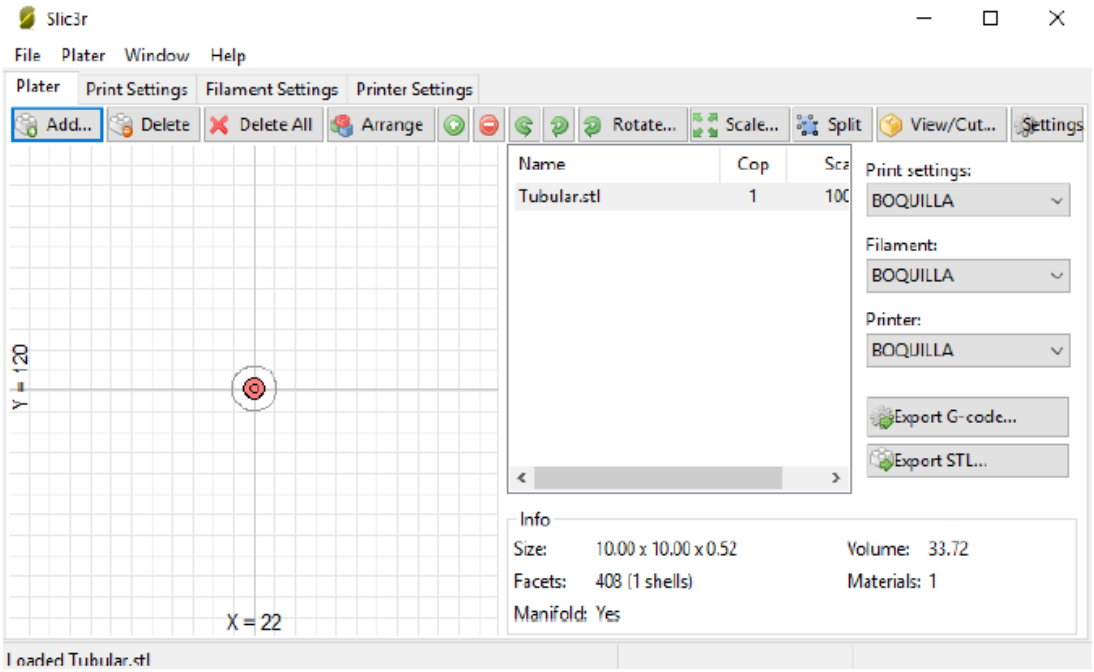

Figure B.0.1. *Main display of Slic3r.*

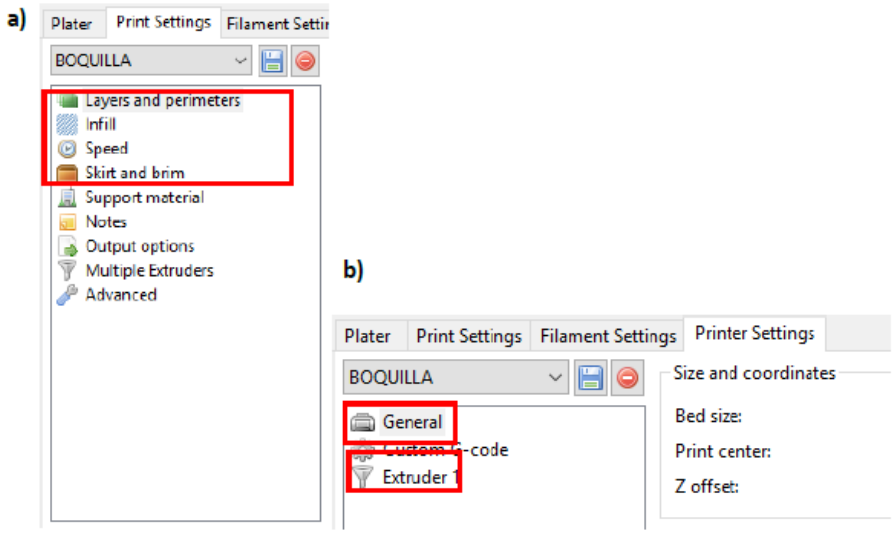

Figure B.0.2. *Both main menus of the principal parameters. a) Main menu of the Print Settings. b) Main menu of the Printer Settings.*

Annex B.2: ImageJ

Available: https://imagej.nih.gov/ij/, visited 16/12/2019

ImageJ is an image processing and analysis software written in Java, which allows it to run on Linux, Mac OS X and Windows, in both 32-bit and 64-bit modes. ImageJ and its Java source code are freely available and in the public domain. No license is required.

In this Master's thesis this software is used to measure and for image processing in order to characterize the porosity and the grain size of the samples.

In the following part, a brief explanation of these two applications will be presented.

A. Measure: This application is used to measure different parameters of an image.

a. Select the option to make lines in the picture (**Figure B.0.3**) and draw a line in the scale line, click in *Ctrl+D*.

b. After that go to *Analyze* (***Figure B.0.3.c***) and chose *Set scale*. A new window will open (see ***Figure B.0.4.b***).

c. In the new window the part of *Know distance*, goes the measure of the scale of the treated picture. Then in the part of *Unit of length*, goes the unit of the scale.

d. Finally, with the option of drawing line (***Figure B.0.3.b***) you can draw lines and measure them clicking *Ctrl+M,* and a new window will open with all the measures.

B. Porosity: This application gives to you the option of measure the percentage of porosity of a picture and the measure of this porosity, making a black and white contrast of the picture.

a. Select the option *Image* (***Figure B.0.3.a***), then the option *Adjust* (***Figure B.0.5.a***), after that select *Threshold* (***Figure B.0.5.b***) and finally a window will open to modify the image (***Figure B.0.5.c***).
b. In the new window (***Figure B.0.5.c***) you can modify the contrast as you desire, to contrast the porosity just adjusting the above option, the green one. When you get the image you want, click the button *Apply*.
c. When the contrast image is generated, go to *Analyze* (***Figure B.0.3.c***) and chose the option *Analyze Particles* and a new window will open.
d. In the new window with the default options just choose *Ok*, the programme will generate two new windows; one of the percentages of the black pixels area that represents the porosity and the size of them. The other one is useful.

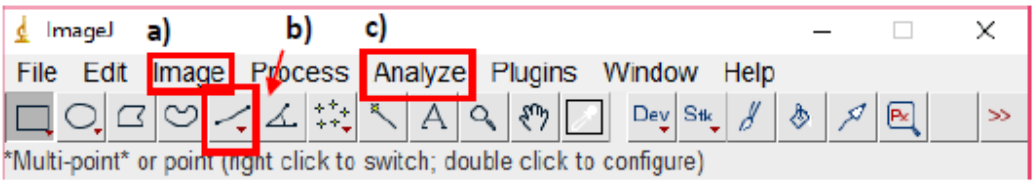

Figure B.0.3. *Principal menu of ImageJ.*

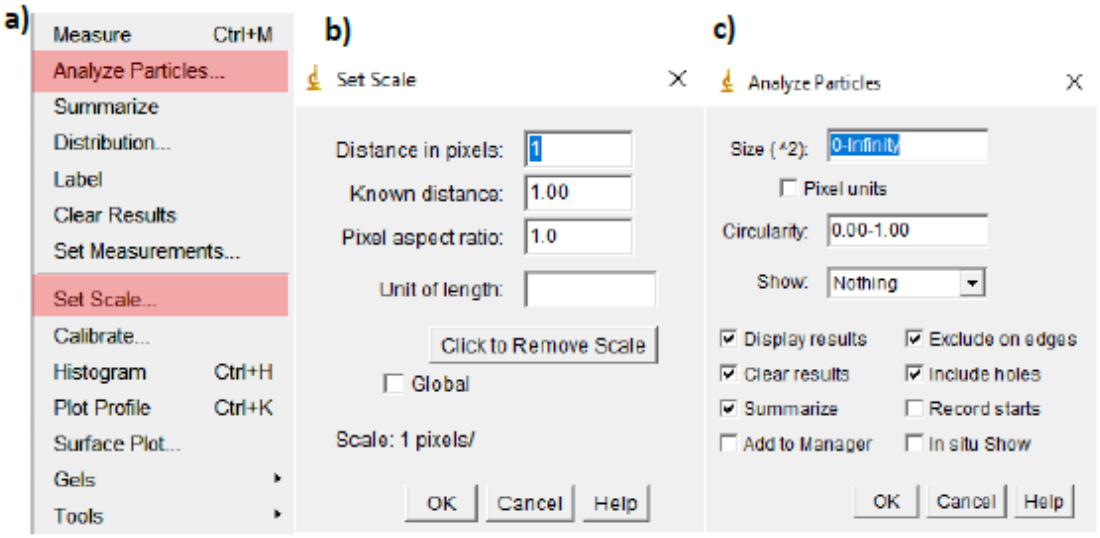

Figure B.0.4. *Analyze menu. a) Main analyze menu. b) Set scale window. c) Analyze particle window.*

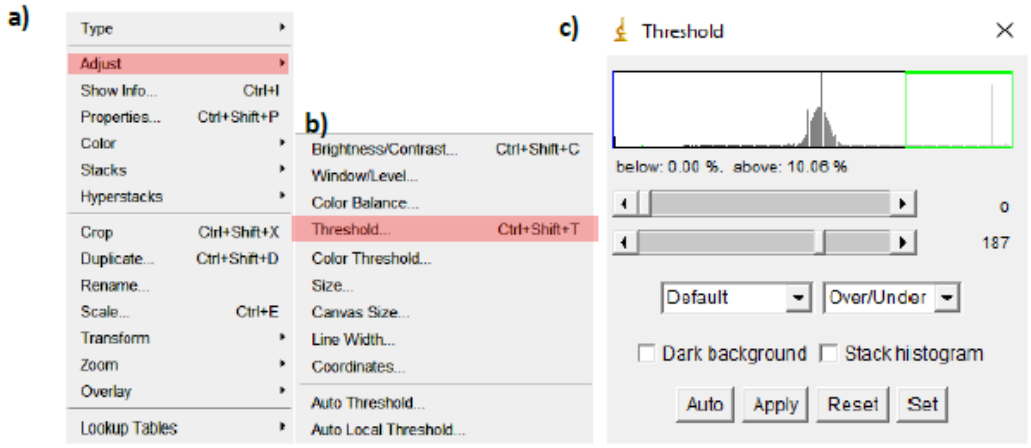

Figure B.0.5. *Image menu. a) Main image menu. b) Adjust menu. c) Threshold window.*

Annex B.3: FreeCad

Available: https://www.freecadweb.org/, visited 27/12/2019.

FreeCAD is an open-source parametric 3D modeler made primarily to design real-life objects of any size. Parametric modelling allows you to easily modify your design by going back into your model history and changing its parameters. *FreeCAD* is a multiplatform (Windows, Mac and Linux), highly customizable and extensible software. It reads and writes to many open file formats such as STEP, IGES, STL, SVG, DXF, OBJ, IFC, DAE and many others.

In this Master's thesis, *FreeCad* is used to design and generate the 3D parts that will be printed.

Annex B.4: Netfabb

Available: https://www.autodesk.com/education/free-software/netfabb, visited 15/12/2019.

Netfabb brings additive design and manufacturing tools together in a single software environment, giving product designers and engineers all the tools they need to optimize, validate and successfully produce models using additive manufacturing processes.

In this Master's thesis this software is used to adjust and perform the STL. file before the *Slic3r* modification. The two main parameters are the centred of the figure and the correction of triangularization of the shape.